Journal of Hazardous Materials 410 (2021) 124562

Contents lists available at ScienceDirect

Journal of Hazardous Materials

journal homepage: www.elsevier.com/locate/jhazmat

Research paper

Photocatalytic and biocidal activities of $ZnTiO_2$ oxynitride heterojunction with MOF-5 and g-C_3N_4: A case study for textile wastewater treatment under direct sunlight

Sherif A. Younis [a,b,f,*], Philippe Serp [c], Hussein N. Nassar [d,e,f]

[a] Analysis and Evaluation Department, Egyptian Petroleum Research Institute, Nasr City, Cairo 1172, Egypt
[b] Central Laboratories, Egyptian Petroleum Research Institute, Nasr City, Cairo 11727, Egypt
[c] Laboratoire de Chimie de Coordination UPR CNRS 8241, Composante ENSIACET, Université de Toulouse, UPS-INP-LCC, 4 Allée Emile Monso, BP 44362, 31030 Toulouse Cedex 4, France
[d] Petroleum Biotechnology Lab., Department of Process Design and Development, Egyptian Petroleum Research Institute (EPRI), Nasr City, Cairo 11727, Egypt
[e] Center of Excellence, October University for Modern Sciences and Arts (MSA), 6th of October City, Giza, PO 12566, Egypt
[f] Nanobiotechnology Program, Faculty of Nanotechnology for Postgraduate Studies, Cairo University, Sheikh Zayed Branch Campus, Sheikh Zayed City, Giza, PO 12588, Egypt

ARTICLE INFO

Editor: Dr. L. Eder

Keywords:
Zinc-titanium oxynitride
Metal-organic framework
Carbon nitride
Textile wastewater treatment
Biocidal activity

ABSTRACT

The work aimed to synthesize three heterojunction photocatalysts (E_g = 2.65–2.78 eV) via in-situ encapsulation of 5% zinc doped titanium oxynitride ($Zn_{0.05}TiO_xN_y$) catalyst into MOF-5 and bulk (BCN)/sulfur-doped (SCN) g-C_3N_4 supports using a microwave method. The prepared photocatalysts were characterized and utilized to purify textile industrial wastewater from the organic dye (e.g., methylene blue, MB) and microbial (e.g., *E. coli, S. aureus*, and *C. albicans*) contaminants under dark, visible, and solar lights. The output data confirmed the higher activity of $Zn_{0.05}TiO_xN_y$@SCN and $Zn_{0.05}TiO_xN_y$@MOF-5 for photo-induced microbial growth inactivation (> 90%) under visible light, with photo-biocidal efficiency of 0.91–1.69 mCFU/Einstein. Such a phenomenon is ascribed to the synergism between the high antimicrobial capacity of supports and photoactivity of $Zn_{0.05}TiO_xN_y$. Also, $Zn_{0.05}TiO_xN_y$@SCN exhibited far superiority to mineralize MB dye (K_{photo} of 2.73 × 10^{-2} min^{-1}) under direct sunlight due to its high photonic (ζ% of 4.4–8.3%)/quantum (QE of 0.56–0.54%) efficiencies for the generation of hydroxyl and superoxide ($^{\bullet}O_2^-$/•OH) oxidative species. As a practical case study, all heterojunction photocatalysts also demonstrated high-performance stability (5 cycles) for real textile wastewater treatment under sunlight (efficiency = 76.1–84.6%).

1. Introduction

A vast amount of wastewater effluents are daily produced worldwide from textile, cosmetics, paper, rubber, leather, and printing industries. Most effluents generated from these industries are released directly into the natural ecosystem without adequate purification, especially from dyestuff industries (Pattnaik et al., 2018). Note that these discharged organic dyes can enrich the microbial contaminant in aquatic systems. Besides, the continuous contamination of natural ecosystems with such contaminants (microbial pathogens and organic dyes) directly impacts the availability of clean freshwater sources for safe drinking due to the high water solubility and toxicity of discharged organic dyes (Tian et al., 2019). Therefore, the development of a green and sustainable method for effective treatment of industrial wastewater effluents (e.g., textile industry) is pivotal to alleviate some of the burdens on the availability of globally clean water sources.

To date, extensive efforts have been carried out on removing dyestuff/organic pollutants from wastewaters by adsorption and photocatalysis techniques using various carbon-based composites (Wang et al., 2017), metal-organic frameworks (MOFs) (Reddy et al., 2020), and other composite materials (Yahya et al., 2018). Adsorption has an excellent prospect for scalable industrial wastewater treatment with many benefits, including energy-saving, ease of operation, high efficiency, and wide-ranging availability (Li et al., 2019). However, the deactivation of microbial pathogens in aqueous streams is far from being optimal by adsorption technique alone. On the other hand,

* Corresponding author at: Analysis and Evaluation Department, Egyptian Petroleum Research Institute, Nasr City, Cairo 1172, Egypt.
E-mail addresses: sherifali_r@yahoo.com (S.A. Younis), philippe.serp@ensiacet.fr (P. Serp).

https://doi.org/10.1016/j.jhazmat.2020.124562
Received 10 August 2020; Received in revised form 19 October 2020; Accepted 10 November 2020
Available online 18 November 2020

photocatalysis possesses the merits of wastewater purification from organic and microbial contaminants via catalytic oxidation mechanism (Dong et al., 2020). Nonetheless, the practical applicability of traditional semiconductor photocatalysts in the field of wastewater treatment is limited due to the possible secondary pollution by intermediates generated during the incomplete oxidation process and poorly visible photon-absorption (≈ 45% of solar spectrum) (Liu et al., 2020). To overcome this limitation, it is recommended to design solar-driven photo-active materials that possess the high capacity to achieve complete removal of microbial/organic pollutants by synergistic adsorption/photocatalytic treatment techniques under dark and sunlight conditions.

The design and engineering of solar-driven photoactive sorbent materials is an attractive eco-friendly clean technology of the 21st century for the real industrial wastewater treatment under day/night conditions. Among photocatalysts, TiO_2 has attracted particular attention in wastewater treatment because of its eco-friendliness, commercial availability (Degussa P-25) at low-cost price (e.g., 1800–2500 USD/Ton, Loman Chemical Co. LTD., China), and high photostability (Fatima et al., 2019). However, the potential applicability of TiO_2 for practical environmental application is still restricted due to its poor-visible light absorption (bandgap energy of Eg ≈ 3.1–3.2 eV; i.e., only excited under UV light), fast electrons-holes (e^-/h^+) recombination (low quantum yield), and poor adsorbability for most organic pollutants. In light of these drawbacks, numerous strategies have been made to upshift the optical response of TiO_2 from the UV to the visible-region via (i) doping/coupling with nitrogen (e.g., TiO_xN_y oxynitride (Aoki et al., 2019)) or metal ions (e.g., zinc-doped TiO_2: Zn_xTiO_2; Deng et al., 2019) and (ii) heterojunction/composite design with metal oxide (e.g., ZnO/TiO_2; Pérez-larios et al., 2012), carbon-based materials (like graphitic-carbon nitride g-C_3N_4/TiO_2; Caudillo-Flores et al., 2019), or metal-organic frameworks (MOFs: TiO_2/MOF-5; Yang et al., 2019). However, so far, these designed photocatalysts still displayed unsatisfactory photocatalytic activities under visible light, with little knowledge about their photocatalytic behaviors under incident sunlight. Hence, efforts are still needed to develop new solar-response photocatalysts with improved photocatalytic/adsorption activities in sunlight.

Based on the band-engineering concept, it is believed that the development of binary heterojunction materials through gathering of the above two strategies (i.e., encapsulation of Zn-doped TiO_xN_y ($ZnTiO_xN_y$) oxynitride photocatalyst onto g-C_3N_4 or MOF-5) can be suggested as an ideal route to improve the synergistic effect of adsorption-enriched solar-induce photocatalysis for real wastewater treatment under direct sunlight. This suggestion is assumed based on the reported adsorption, optical, and antimicrobial activities of pristine g-C_3N_4 and MOF-5. For example, the use of g-C_3N_4 (E_g ≈ 2.7–2.8 eV) has attracted much attention as a metal-free visible-driven photocatalyst with high adsorption capacity for various dye organic pollutants in water matrices (Liu et al., 2020; Younis et al., 2016). More importantly, sulfur-doped g-C_3N_4 (SCN) was shown to improve significantly charge mobility and e^-/h^+ pair separation compared to bulk g-C_3N_4 (BCN) due to the upshifting of the valence band position (Oh et al., 2018). Additionally, MOFs have been suggested as potential biocides with antimicrobial properties, especially those containing zinc metal sites (e.g., MOF-5, also known as IRMOF-1) (Martín-Betancor et al., 2017). In particular, MOF-5, with Zn_4O metal clusters, is a UV-driven photocatalyst in which the organic ligands (BDC = benzene-1,4-dicarboxylic acid) act as antennas to harvest photon light and activate Zn_4O catalytic site through a localized ligand-to-metal cluster charge transfer (LMCT) mechanism (Younis et al., 2020). Because of the high surface-to-volume ratio and tunable porosity of MOF-5 along with its framework flexibility, it was also utilized as an effective sorbent for many organic/inorganic pollutants in aqueous solutions (Mirsoleimani-azizi et al., 2018; Bakhtiari and Azizian, 2015). However, the pure MOF-5 is unstable upon exposure to moisture and aqueous solution, limiting its application for practical wastewater treatment (Chu et al., 2018). As one of the most promising options to overcome this limitation, the design of MOF-based composites has been widely recommended to improve MOF water stability as well as visible-driven photocatalysis (Jiang et al., 2018).

Accordingly, in this work, three binary heterojunctions materials are prepared through in-situ encapsulation of $ZnTiO_xN_y$ oxynitride nanoparticles (NPs) in MOF-5, bulk g-C_3N_4, and sulfur-doped g-C_3N_4 using a fast microwave procedure. A detailed characterization of the prepared heterojunctions ($ZnTiO_xN_y$@MOF-5, and $ZnTiO_xN_y$@BCN, or $ZnTiO_xN_y$@SCN) was performed to understand their surface chemistry, crystallographical-, morphological-, textural-, and optical-properties relative to the original materials. Followed that, the adsorption, photocatalytic, and biocidal performances of the synthesized photocatalysts were investigated and compared towards the elimination of methylene blue (MB) dye and three microbial pathogens [Gram-negative *Escherichia coli* ATCC 8739, Gram-positive *Staphylococcus aureus* ATCC 25923, and the yeast *Candida albicans* ATCC 10231] from synthetic wastewater solutions under different light sources (dark, ultraviolet, LED visible, and sunlight). These bacterial/yeast strains were selected as representative for the predominant microbial diversity in textile effluents and surface water. Besides, the photocatalysis mechanism was also examined by determining: (i) the dominant reactive oxidative species (ROS), and (ii) the main intermediates generated during photocatalytic degradation of organic dye pollutants. The reusability and the effectiveness of the prepared hybrid photocatalysts in treating real industrial textile wastewater (in terms of chemical oxygen demand (COD, mg/L)) were also evaluated to assess their performances under real-conditions. Thus, it is expected that the results obtained in this work would offer useful information toward the synthesis of bifunctional materials for efficient purification of industrial/surface wastewater from various organic/microbial pollutants via the synergism between adsorption and photocatalysis in a one-cleaning treatment step.

2. Experimental procedures

2.1. Preparation of $Zn_{0.05}TiO_xN_y$ encapsulated in g-C_3N_4 and MOF-5 supports

By using the microwave synthesis method, both bulk graphitic (BCN) and sulfur-doped carbon nitride (SCN) sheets were prepared from urea and thiourea as starting nitrogen-rich precursors (Younis et al., 2016), while MOF-5 was synthesized from the coordination of zinc ion with benzene-1,4-dicarboxylic acid (BDC) precursor (Choi et al., 2006). The preparation of 5% Zn doped TiO_xN_y oxynitride ($Zn_{0.05}TiO_xN_y$) nanoparticles (NPs) was carried out by a two-step hydrothermal method using a diluted Zn/Ti elements (Zn/Ti ≈ 0.05) in ethanol/nitric acid solution mixture and 1% aqueous urea solution as a nitrogen source. The detailed synthesis procedures of pure BCN, SCN, MOF-5, and $Zn_{0.05}TiO_xN_y$ NPs are illustrated in the electronic supplementary information (ESI: Section S1). By following the same synthesis procedure of pure $Zn_{0.05}TiO_xN_y$ NPs, the in-situ growth of $Zn_{0.05}TiO_xN_y$ NPs was carried out in the presence of 67 wt% of g-C_3N_4 sheets (BCN or SCN) to prepare $Zn_{0.05}TiO_xN_y$@BCN or $Zn_{0.05}TiO_xN_y$@SCN hybrid structures. On the other hand, the microwave-assisted growth of cubic MOF-5 crystals was performed in the presence of 33 wt% of $Zn_{0.05}TiO_xN_y$ NPs to design $Zn_{0.05}TiO_xN_y$@MOF-5 heterostructure. Scheme 1 represents the microwave synthesis procedures for BCN, SCN, MOF-5, and $Zn_{0.05}TiO_xN_y$ oxynitride NPs and their corresponding hybrid photocatalysts (e.g., $Zn_{0.05}TiO_xN_y$@BCN, $Zn_{0.05}TiO_xN_y$@SCN, and $Zn_{0.05}TiO_xN_y$@MOF-5).

All the prepared materials (single and binary photocatalysts) were characterized by various techniques to evaluate their crystalline, chemical, textural, morphological, thermal, and optical properties, as illustrated in the electronic supplementary information file (ESI: Section S1.4). The characterization techniques include X-ray diffraction (XRD), X-ray photoelectron spectroscopy (XPS), Fourier transform infrared

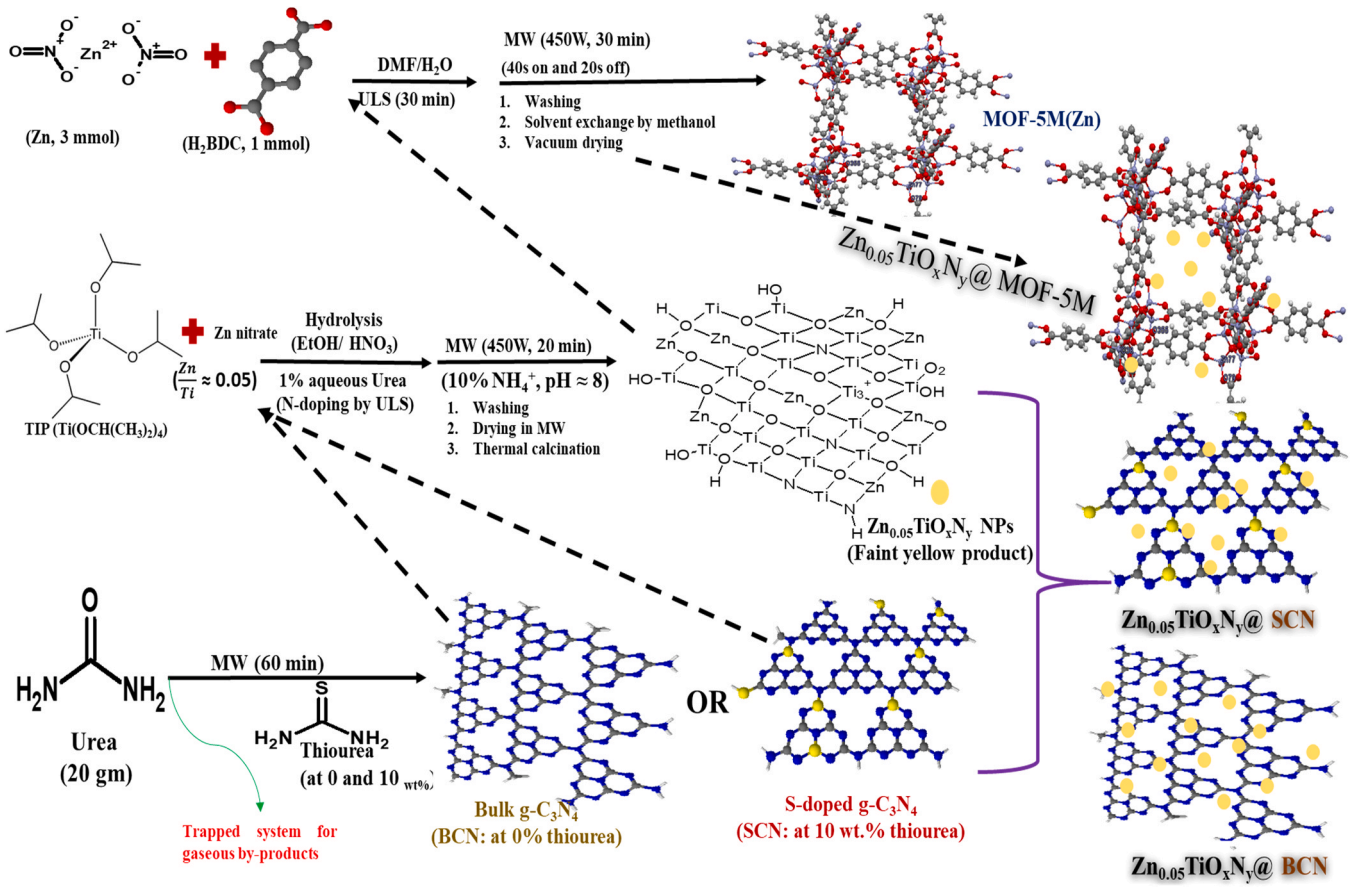

Scheme 1. Schematic diagram for tailoring the preparation of $Zn_{0.05}TiO_xN_y$@MOF-5, $Zn_{0.05}TiO_xN_y$@BCN, and $Zn_{0.05}TiO_xN_y$@SCN heterostructures and their corresponding pristine photocatalysts.

spectroscopy (FTIR), field-emission scan electron microscopy (FESEM) equipped with energy-dispersive X-ray spectroscopy (EDX), transmission electron microscopy (TEM), Raman spectroscopy, thermogravimetric analysis (TGA), UV–visible diffuse reflectance spectroscopy (UV–Vis DRS), photoluminescence (PL) spectroscopy, N_2 adsorption-desorption isotherm, CHNS-analyzer, and inductively coupled plasma-mass spectrometry (ICP-MS).

2.2. Experimental application studies

2.2.1. Adsorption/photocatalytic treatment process

Two types of wastewaters were used to evaluate the photocatalytic/adsorption performances of the prepared photocatalysts, including synthetic wastewater contaminated with 80 μmol/L methylene blue dye (MB, as a model pollutant) and real industrial textile effluent collected from one of the spinning and weaving industries in Egypt (2018). The physicochemical characteristics of the real wastewater were determined in terms of effluent pH, total dissolved salts (TDS), chemical oxygen demand (COD), and biochemical oxygen demand (BOD_5) in compliance with the Standard Methods for the Examination of Water and Wastewater (Ertugay and Acar, 2017).

The adsorption/photocatalytic treatment processes for water samples were carried out in a batch type cylindrical reactor (150 mL volume) molded with a double-wall for temperature controller at 25 °C. First, 1 g/L of each photocatalyst was dispersed into 100 mL of wastewater solution (pH 6.5 ± 0.3) containing 1248 mg/L total dissolved solids (e.g., NaCl, KCl, $Ca(HCO_3)_2$, $MgCl_2$, and Na_2SO_4). Before light irradiation, the suspended solution was stirred (at 150 rpm) in the dark for 180 min to evaluate the adsorption process. After that, the suspension solution was subjected to the light irradiation so as to initiate the photocatalytic process. During photocatalysis, a continuous air stream was injected into the reaction system (50 mL/min flow rate) to maintain dissolved oxygen at 7.05 mg/L for the oxidation reaction. Three light sources were employed during the photocatalytic tests: (i) UVC ultraviolet-light (HPK 125 W high-pressure mercury vapor lamp, λ_{max} = 253 nm), (ii) incident visible-light (two Philips indoor luminaires, MASTER TL-D Super 80 36 W/840; λ_{max} ≈ 420~650 nm), and (iii) direct sunlight (a summer day between 11.00 am and 4.00 pm; i.e., the light intensity in a typical sunny day is in the range of 1.5–2 kW/m^2). The visible lamps were placed over the photoreactor vessel at a distance of around 5–7 cm, while the depth of wastewater solution during the photocatalytic treatment was maintained at around 10 cm. At regular time intervals, 2 mL of the treated water sample was withdrawn and filtrated with a 0.45 μm PTFE Millipore membrane to determine the residual concentration of MB dye against blank photolysis (without photocatalyst). The measurement of MB dye concentration in solution was done using a double beam UV–visible spectrophotometer (λ_{max} = 668 nm), with a minimum detection limit of 0.25 μmol/L. The treated solution's COD (mg/L) value was determined by a closed reflux colorimetric method using COD Hack vials [0–1500 mg O_2/L] at λ_{max} = 610 nm (Ertugay and Acar, 2017). The photo-remediation efficiency (R %: Eq. S1) and adsorption capacity ($\mathbf{q_t}$, μmol/g: Eq. S2) were calculated in duplicate to verify the experimental errors (<6.75%). In detail, experimental kinetic modeling equations are described in the supplementary information (ESI: S1.5 and Table S1).

2.2.2. Biocidal and photo-disinfection of pathogenic microbes in aqueous solution

The biocidal and disinfection activities against the three microbial pathogens (*E. coli*, *S. aureus*, and *C. albicans* yeast) were carried out using

the standard plate count method. In this procedure, Luria Broth (LB) media containing 1 g/L of each photocatalyst, based on the minimum inhibitory concentration, were initially prepared and sterilized at 120 °C for 30 min. After cooling, the sterilized LB broth media were injected with freshly grown axenic culture (10^5 cells/mL: 50 mL) and incubated under visible-light (72 W tungsten lamp with intensity ≈ 390 W/m^2, using a UV cutoff filter $> \lambda_{max} \approx 450$ nm) for 48 h at 37 °C under shaking speed of 150 rpm. The survived (viable) microbial cells in the LB samples were counted at different time intervals (as a colony-forming unit: CFU/mL) on nutrient agar plates. Three replicates and negative control (without photocatalyst) were simultaneously tested for each run to evaluate the experimental errors and the light source's effect on the inhibition rates. The photo-biocidal efficiency of the photocatalysts under visible-light was determined using the following equation (Eq. 1):

$$\textbf{Photo} - \textbf{biocidal} \quad \textbf{efficiency}_{\%} = \left[\frac{CFU_o - CFU_T}{CFU_o}\right] \times 100 \tag{1}$$

The biocidal experiments were also carried out under dark conditions (keeping all other parameters identical for comparison) to determine the antimicrobial capacity of the prepared materials. In this case, the antimicrobial efficiency was determined using the following formula (Eq. 2):

$$\textbf{Antimicrobial} \quad \textbf{efficiency}_{\%} = \left[\frac{CFU_N - CFU_d}{CFU_N - CFU_p}\right] \times 100 \tag{2}$$

where CFU_o and CFU_T are the recorded CFU/mL before and after incubation with photocatalysts, respectively. CFU_d is the number of viable cells after biocidal treatment in dark light. CFU_p (a positive control) is the count of the microbial cells treated with isopropyl alcohol (70% v/v: as standard antimicrobial activity agent), whereas CFU_N (a negative control) is the count of the microbial cells without any treatment.

To understand the effect of light intensity on the disinfection rate, the kinetic of disinfection (dark/light) was studied based on the classical pseudo-first-order-kinetic given by Chick and Watson model (ESI: Table S1) (Nair et al., 2011; Das et al., 2015). Furthermore, microbicide photonic efficiency (MPE) was also determined based on the concept of photonic detoxification efficiency (ε_{mb}: Eq. 3) (Nair et al., 2011).

$$\varepsilon_{mb} = \Delta N / J A_p \Delta t \tag{3}$$

where ΔN is the change in CFU in the active platting area (A_p, m^2); **J** is the photon flux [$\mathbf{J} = I\lambda/N_A hc$ in Einstein/m^2/s: as **I** = light intensity of 390 W/m^2, $\boldsymbol{h}$ = Planck's constant (J/s), $\mathbf{N_A}$ = Avogadro constant, **c** = speed of light (m/s)], and Δt is the change in time (s).

The apparent quantum efficiency (QE: Eq. 4) of the prepared photocatalysts was also calculated to evaluate the photocatalytic performance (Younis et al., 2020).

$$QE = \frac{\text{Decay rate(photoreacted molecules per second)}}{\text{Photon flux(Photon per second)}} \times 100 \tag{4}$$

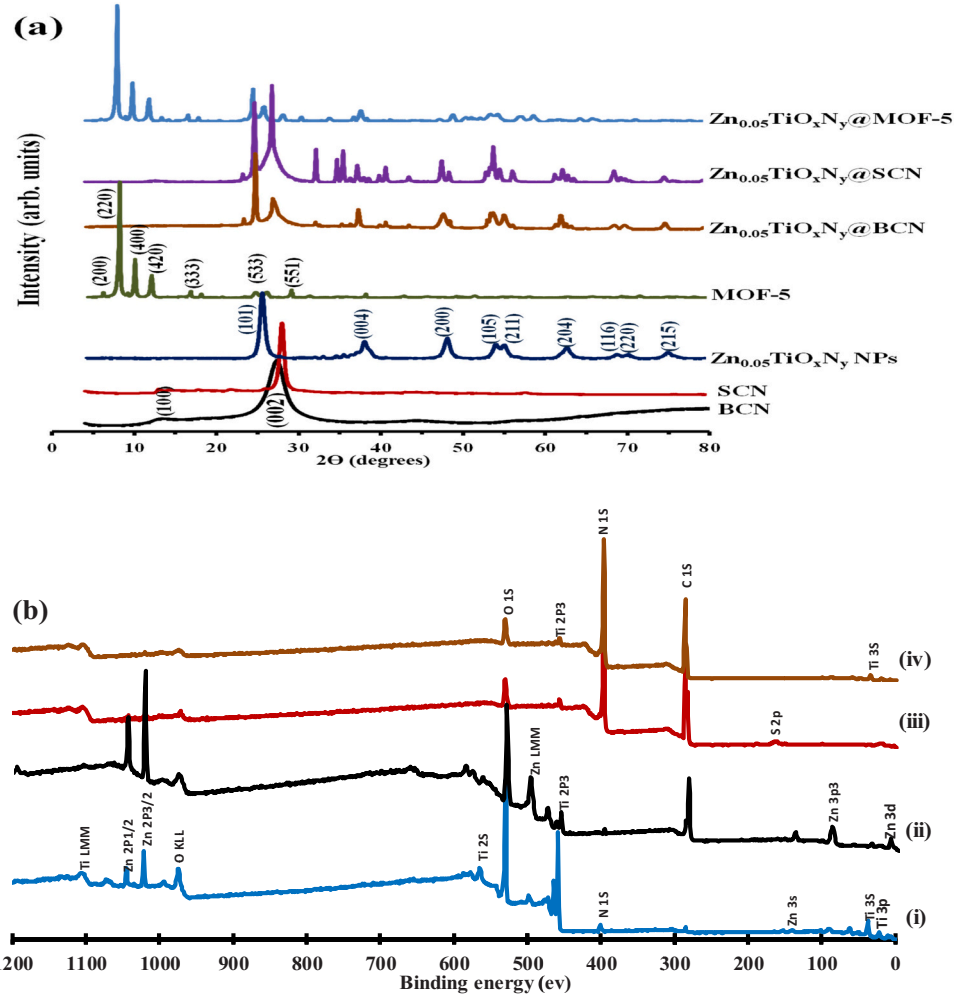

Fig. 1. (a) XRD patterns of the single and hybrid materials (BCN, SCN, $Zn_{0.05}TiO_xN_y$, MOF-5, $Zn_{0.05}TiO_xN_y$@BCN, $Zn_{0.05}TiO_xN_y$@SCN, and $Zn_{0.05}TiO_xN_y$@MOF-5) and (b) XPS spectra of bare $Zn_{0.05}TiO_xN_y$ NPs (i) with respect to hybrid photocatalysts [(ii)- $Zn_{0.05}TiO_xN_y$@MOF-5, (iii)- $Zn_{0.05}TiO_xN_y$@SCN, and (iv)- $Zn_{0.05}TiO_xN_y$@BCN].

3. Results and discussion

3.1. Characterization data

3.1.1. Crystalline phases and chemical properties

Fig. 1 shows the XRD diagrams and XPS spectra of the prepared photocatalysts. In Fig. 1(a), the XRD peaks of the pure MOF-5 (at $2\Theta = 0.9^\circ$ (200), 9.8° (220), and 24.9° (551)) and $Zn_{0.05}TiO_xN_y$-oxynitride (at $2\Theta = 25.4^\circ$ (101) and 48.04° (200)) confirmed the obtention of cubic crystalline phase of $Zn_4O(BDC)_3$ (space group: *Fm-3m*) and an isostructural of TiO_2 anatase structure (body-centered tetragonal crystal), respectively (Hao et al., 2018; Grasset et al., 2007). Compared with the pure TiO_2 anatase phase [JCPDS Card no. 78-2486], the XRD patterns of $Zn_{0.05}TiO_xN_y$-oxynitride showed low-intensity peaks in the region $25.5^\circ < 2\theta < 37^\circ$ due to the cation deficiency in the anatase phase as a result of the substitution of host Ti^{4+} (0.605 Å) and O^{2-} (1.4 Å) ions by Zn^{2+} (0.74 Å) and N^{3-} (0.13 Å) dopants (Grasset et al., 2007). The XRD data of BCN and SCN materials showed a typical pattern of g-C_3N_4 sheets, with two peaks at $2\Theta = 13.25$–13.4° (001) and 27.3–28.13° (002) for the in-plane repeated units of tri-s-triazine (heptazine framework) and the interplanar stacking, respectively (Younis et al., 2016; Wang et al., 2015). However, the interlayer spacing (d_{002}) decreases slightly in SCN (0.317 nm) compared to BCN (0.336 nm) due to the electron localization of the sulfur atom in the SCN, which makes stronger binding between the heptazine layers (Yang et al., 2017). For the hybrid photocatalysts in Fig. 1(a), the XRD patterns of $Zn_{0.05}TiO_xN_y$@MOF-5, $Zn_{0.05}TiO_xN_y$@BCN, and $Zn_{0.05}TiO_xN_y$@SCN heterojunctions showed well-matched diffraction peaks to their corresponding individual components, confirming their successful synthesis without alteration in the crystalline phases after hybridization. Only $Zn_{0.05}TiO_xN_y$@SCN showed an overlap for the (100) plane of SCN and the (101) plane of $Zn_{0.05}TiO_xN_y$, along with a few unidentified peaks at 2Θ of 22.0–40.0°. This observation could be attributed to the reaction of sulfur species with the $Zn_{0.05}TiO_xN_y$ network during microwave synthesis, which may induce some alterations of atomic orientations within the $Zn_{0.05}TiO_xN_y$ crystal structure.

In Fig. 1(b), the XPS survey spectra confirmed the successful synthesis of $Zn_{0.05}TiO_xN_y$ photocatalyst and its composites with MOF-5, BCN, and SCN supports. In general, the XPS data confirmed the presence of two oxidation states for titanium (Ti^{4+} $2p_{3/2}$ and Ti^{3+} $2p_{3/2}$ at binding energy (BE) of 459.20 and 458.5 eV, respectively) in the prepared $Zn_{0.05}TiO_xN_y$ photocatalyst (Fig. 1b (i)). TheTi^{4+}/Ti^{3+} oxidation states can be explained by the formation of oxygen vacancies resulting from (i) the replacement of Ti^{4+} in TiO_2 crystal by Zn^{2+} cation (i.e., Zn-O bonding (Fig. S1(c)), with BE of 1021.9 for Zn $2p_{3/2}$) (Grasset et al., 2007; Mitra et al., 2017) and/or (ii) the substitutional doping of nitrogen atom (at BE of 399.4 eV) in the crystal structure (Ferrari-Lima et al., 2015; Kadam et al., 2017). For the hybrid photocatalysts, the XPS survey spectrum of $Zn_{0.05}TiO_xN_y$@MOF-5 (Fig. 1b (ii)) indicates the presence of Ti^{4+}/Ti^{3+} *2p* (BE at 458.3–467.48 eV) and N *1 s* (BE at 399.4 eV) peaks related to the incorporation of $Zn_{0.05}TiO_xN_y$ NPs within the MOF-5 framework. The photoelectron peaks of $Zn_{0.05}TiO_xN_y$@MOF-5 elemental constituents were as follows (Fig. 1b (ii)): Zn *2p* (BE at 1021.8–1025.9 eV), Ti *2p* (BE at 458.3–467.48 eV), C *1s* (BE at 284.6–291.38 eV), N *1s* (BE at 399.4 eV), and O *1s* (BE at 531.59–535.78 eV). Likewise, both Zn *2p* (BE at 1021.8–1025.9 eV) and Ti *2p* (BE at 458.2–467.5 eV) peaks were observed in the XPS survey spectra of $Zn_{0.05}TiO_xN_y$@BCN (Fig. 1b (iii)) and $Zn_{0.05}TiO_xN_y$ @SCN (Fig. 1b (vi)) composites. Besides, the $Zn_{0.05}TiO_xN_y$@SCN spectrum shows the S *2p* peak (Fig. S1(g)), which can be fitted into two core level peaks at BE of 164.4 eV (C=S bond) and 167.8 eV (S=O species) (You et al., 2017). Moreover, the deconvolution of C *1s* and N *1s* regions (Fig. S1) confirmed the presence of the graphitic C–N network within both $Zn_{0.05}TiO_xN_y$@BCN and $Zn_{0.05}TiO_xN_y$@SCN hybrid photocatalysts (details in the ESI: section S2.1).

The above-mentioned characteristic results were further verified by the FTIR, Raman, and TGA analyses, as shown in Figs. S2 and S3 (ESI). In brief, the overturned FTIR peaks at 1100 − 1150 cm^{-1} are ascribed to the vibrations of O–Ti–N, N–Ti–N, and Zn–O–Ti bonds within $Zn_{0.05}TiO_xN_y$ NPs incorporated into all hetero-structured photocatalysts (Fig. S2(a)) (Qiao et al., 2016; Etacheri et al., 2010). The Ti^{3+}–OH vibration peak of $Zn_{0.05}TiO_xN_y$ NPs was also observed at 3840 cm^{-1} in all the heterostructures, indicating the successful synthesis of hybrid photocatalysts (Qiao et al., 2016). In Fig. S2(b), the typical active vibrations for the $Zn_{0.05}TiO_xN_y$ anatase phase were observed in all the heterostructures with an up-field Raman shift (E_g, $B_{1\,g}$, A_{1g}, and E_g symmetries at 144, 197, 396, 513, and 640 cm^{-1}, respectively). The notable change in the intensities with a substantial up-field shift in Raman vibrational modes could be attributed to a hybrid structure without change on phase purities (details in the ESI: section S2.1). Moreover, based on the TGA plots (Fig. S3), the prepared $Zn_{0.05}TiO_xN_y$@SCN, $Zn_{0.05}TiO_xN_y$@BCN, and $Zn_{0.05}TiO_xN_y$@MOF-5 heterojunctions showed increased thermal stability (relative to pristine materials), with recorded weight loss of about 2.6%, 4.1%, and 49.8%, respectively at 495 °C. The increased thermal stability of hybrid photocatalysts can be ascribed to the presence of 33 wt% $Zn_{0.05}TiO_xN_y$ NPs (as a thermally stable catalyst with <1.5% weight loss at 850 °C) in all the structures. Among pristine samples, MOF-5 had the lowest thermal stability (58.6% weight loss at 478 °C) due to BDC ligand's thermal decomposition along with Zn metal centers' conversion to ZnO NPs end products (Hafizovic et al., 2007). Also, the SCN sheets demonstrate higher thermal-stability (1.8% weight loss at 545 °C) than the BCN (2.4% weight loss at 478 °C), resulting from the increased stability of heptazine-base units in the presence of sulfur dopant within the carbon nitride sheet (Elshafie et al., 2020).

3.1.2. Morphological and textural properties

The surface morphology of the synthesized materials was characterized by TEM and FESEM techniques, as shown in Figs. S4 and S5 (ESI). The TEM images of the individual materials (Fig. S4) show a 2D layered sheet-like morphology for BCN and SCN (Fig. S4 (a–b)) (Ke et al., 2017), spherical-shaped nanoparticles for $Zn_{0.05}TiO_xN_y$ (DLS particle size ranging from 6 to 34 nm, Fig. S4 (c)), and a 3 D cubic structure for MOF-5 (particle size distribution from 1.3 to 4.8 μm, Fig. S4(d)) (Bakhtiari and Azizian, 2015). In the case of the hybrid photocatalysts, FESEM images (Fig. S5 (a–c)) also show that the spherical-shaped $Zn_{0.05}TiO_xN_y$ NPs are distributed uniformly within the 2D/3D layers of BCN, SCN, and MOF-5 supports. The overall elemental analysis data (using EDX, CHNS analyzer, and ICP-MS, ESI: Section S2.1.3) also verified that approximately 32.3 ± 1.9% w/w of $Zn_{0.05}TiO_xN_y$ NPs were successfully encapsulated in the three supports (BCN, SCN, and MOF-5). This measured value is close to the theoretical one (33% w/w), indicating the successful synthesis of the three hetero-structured photocatalysts with the proposed chemical constituents using the in-situ impregnation method.

The prepared photocatalysts' textural properties based on the N_2-adsorption/desorption isotherm at 77 K are listed in Table 1. The surface area (S_{BET}) and pore volume (V_{total}) of pristine MOF-5 and SCN materials decreased after hybridization with $Zn_{0.05}TiO_xN_y$ NPs. In contrast, the encapsulation of $Zn_{0.05}TiO_xN_y$ caused a significant increase in the average pore size (D_p) of all hybrid photocatalysts ($Zn_{0.05}TiO_xN_y$@MOF-5, $Zn_{0.05}TiO_xN_y$@SCN, and $Zn_{0.05}TiO_xN_y$@BCN; with D*p* of 3.4–7.4 nm) relative to their corresponding pristine materials (D_p of 2.9–4.4 nm). However, it should be noted that all the determined D_P values confirms the formation of mesoporous photocatalysts. Among all hybrid photocatalysts, $Zn_{0.05}TiO_xN_y$@MOF-5 has the highest surface area (S_{BET} of 904 m^2/g) and pore volume (V_{total} of 0.45 cm^3/g) due to the large surface-to-pore volume of MOF-5 (Table 1). The decreased S_{BET} and V_{total} values for the hybrid photocatalysts (relative to single materials) could be attributed to the partial filling/blocking of mesopores during the in-situ impregnation of $Zn_{0.05}TiO_xN_y$ NPs onto SCN or MOF-5 supports. The increased pore size of hybrid materials could also be linked to:

Table 1
The textural and optical properties of the prepared photocatalyst materials.

Photocatalyst materials	Textural data[1]			Optical data				
	S_{BET} (m^2/g)	Total pore volume (V_{total}: cm^3/g)	BJH pore size (D_P: nm)	Absorption band edge (nm)	Theoretical[2] E_g (eV)	Measured[2] E_g (eV)	CB (eV)	VB (eV)
BCN	36	0.53	4.2	450	2.76	2.81	−1.24	1.58
SCN	86	1.20	4.4	463	2.68	2.78	−1.22	1.56
MOF-5	1291	0.58	3.0	384	3.23	3.23	−0.58	2.66
$Zn_{0.05}TiO_xN_y$ NPs	62	1.07	2.9	449	2.77	2.77	−0.35	2.43
$Zn_{0.05}TiO_xN_y$@BCN	44	0.27	7.4	469	2.65	2.68	–	–
$Zn_{0.05}TiO_xN_y$@SCN	51	0.30	7.4	456	2.72	2.79	–	–
$Zn_{0.05}TiO_xN_y$@MOF-5	904	0.45	3.4	447	2.78	2.83	–	–

[a] The textural properties were determined based on N_2-adsorption/desorption isotherm using Brunauer–Emmett–Teller (BET) and Barrett–Joyner–Halenda (BJH) theories.
[b] The theoretical E_g values are estimated from 1240/wavelength (nm), whereas the measured E_g values are calculated from the Mott–Schottky plots of $(\propto h\nu)2$ vs. $(h\nu)$ using UV–vis DRS results.

(i) the high dispersion of $Zn_{0.05}TiO_xN_y$ on carbon nitride sheets with an increase of bond lengths and porous structures per unit mass, and (ii) the creation of a new interface between $Zn_{0.05}TiO_xN_y$ and carbon nitride sheets as a result of chemical bond formation (between S/N-atoms and Zn/Ti-elements) during the synthesis (Sahoo et al., 2019). At this end, the larger pore size, surface area, and pore volume of $Zn_{0.05}TiO_xN_y$@-MOF-5 could significantly improve its adsorption/photocatalytic performances by efficiently accelerating mass diffusion during the treatment of contaminated wastewater, as verified experimentally in Sections 3.2 and 3.4.

3.1.3. *Optical properties*

Based on the UV–vis DRS spectra (Fig. 2a), the bandgap energy (E_g) of all the synthesized materials (Table 1) were determined using Mott–Schottky plots $[(\propto h\nu)^2$ *vs.* $(h\nu)$; as illustrated in the ESI: Section S2.1.4] (El-Maghrabi et al., 2017). As seen in Fig. 2(a), all the pristine photocatalysts ($Zn_{0.05}TiO_xN_y$, BCN, and SCN) showed a good capability for visible light absorption (wavelength (λ) of 449–463 nm), except

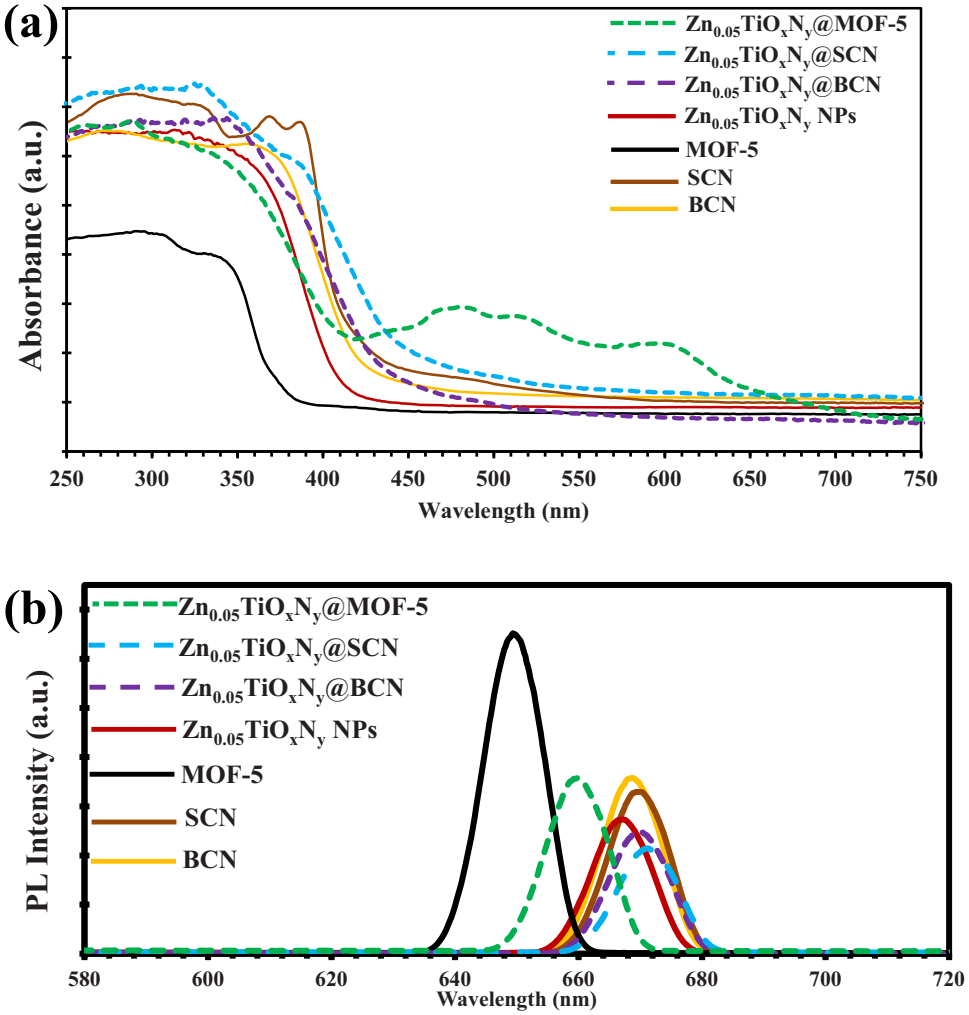

Fig. 2. The optical properties for the synthesized photocatalysts: (a) UV–visible DRS spectra and (b) PL spectra (excitation λ = 335 nm).

MOF-5 with a basal absorption edge in the ultraviolet region (λ at 384 nm). After the hybridization process, all the hetero-structured photocatalysts exhibited up-lift in the visible absorption region of wavelength more than 450 nm. The bandgap energy (E_g) values of $Zn_{0.05}TiO_xN_y$@-MOF-5, $Zn_{0.05}TiO_xN_y$@BCN, and $Zn_{0.05}TiO_xN_y$@SCN were 2.78, 2.72, and 2.65 eV, respectively (Table 1). The UV-light absorption by MOF-5 (E_g of 3.23 eV) can be attributed to the ligand (BDC)-to-(ZnO) metal nodes charge transfer mechanism upon irradiation (Younis et al., 2020). The capability of $Zn_{0.05}TiO_xN_y$ for visible light absorption is in a good agreement with the band-engineering concept (doping of TiO_2 with N and Zn atoms) (Aoki et al., 2019). Accordingly, the improved optical property of the three heterojunctions (relative to the pure materials) can be ascribed to the interfacial charge transfer across the heterojunction between visible-driven $Zn_{0.05}TiO_xN_y$ NPs and the supporting catalysts. This is confirmed by the PL emission spectra (Fig. 2b, excitation at 335 nm), which showed red-shift of fluorescence emission peaks for all the heterostructured photocatalysts compared to the pristine materials. Specifically, the PL emission of $Zn_{0.05}TiO_xN_y$@SCN exhibited the highest quenched intensity (upshifted to 672 nm, Fig. 2b) due to the crystal surface defects (oxygen vacancies) on $Zn_{0.05}TiO_xN_y$ and the reduction of the free charge carrier concentration on the S-doped C_3N_4 (sulfur-doped heptazine in which *S* atoms partially substitute *N*-edges in g-C_3N_4 planes) (Song et al., 2018). Similarly, the PL spectrum of $Zn_{0.05}TiO_xN_y$@MOF-5 exhibited a higher shift in emission peak (≈ 658 nm) with a decreased intensity relative to pure MOF-5 (650 nm; Fig. 2b), indicating an improvement in the migration/separation of photogenerated charges (e^-/h^+ pairs) upon excitation (Zhang et al., 2019; Ma et al., 2016).

To confirm the above-mentioned optical features, the photocatalytic activities of the heterostructured photocatalysts (relative to their single counterparts) were investigated towards textile wastewater treatment under various light sources.

3.2. Photocatalytic activities toward MB dye contaminated wastewater

3.2.1. Effect of the light source

It is well-known that adsorption plays an essential role in improving photocatalytic treatment because it is the initial step for the pre-concentration of organic molecules on the photoactive sites. Hence, the coupled adsorption/photocatalytic activities of the prepared photocatalysts toward removing 80 μmol/L MB dye are shown in Fig. 3. The results revealed that MOF-5 and $Zn_{0.05}TiO_xN_y$@MOF-5 had the fastest adsorption uptake for MB dye (≈42–45%, with capacity (q_e) ≈ 33.2 ± 3.0 μmol g^{-1}) within 60 min in dark condition. In contrast, the photocatalytic performance of $Zn_{0.05}TiO_xN_y$@SCN outperformed all other prepared photocatalysts toward MB dye degradation under all light sources (Fig. 3). The photocatalytic activity of all photocatalysts was found to be dependent on the light source, with the high capability to initiate solar-induced photocatalysis. Under sunlight (for 90 min), the performance of the prepared photocatalysts towards the discoloration of MB dye-contaminated water ranked in the order: $Zn_{0.05}TiO_xN_y$@SCN (95.4%) > $Zn_{0.05}TiO_xN_y$@BCN (91.0%) > SCN (79.1%) ≈ $Zn_{0.05}TiO_xN_y$@MOF-5 (78.0%) > $Zn_{0.05}TiO_xN_y$ (64.5%) > BCN (54.3%) > MOF-5 (53.0%) (details in ESI: Section S2.2). The performances sharply increased under UV light to achieve approximately complete MB dye degradation (> 98% discoloration after 90 min) when using hybrid photocatalysts (as compared to 57–76% discoloration efficiency by all pristine materials, Fig. 3). However, under visible light, the photocatalytic performance of all photocatalysts slightly decreased to about 43.33%, 73.2%, 58.8%, 48.3%, 92%, 83.4%, and 70.5% for BCN, SCN, $Zn_{0.05}TiO_xN_y$, MOF-5, $Zn_{0.05}TiO_xN_y$@SCN, $Zn_{0.05}TiO_xN_y$@BCN, and $Zn_{0.05}TiO_xN_y$@MOF-5, respectively after 90 min. Compared with P25 TiO_2 (as a commercial photocatalyst: Fig. S6 in the ESI), it was apparent that the designed $Zn_{0.05}TiO_xN_y$ NPs significantly improved the adsorption/photocatalytic performances toward MB dye removal under dark/visible conditions. In contrast, the UV-induced photocatalysis by P25 TiO_2 was 1.2-time higher than $Zn_{0.05}TiO_xN_y$ NPs. Specifically, the

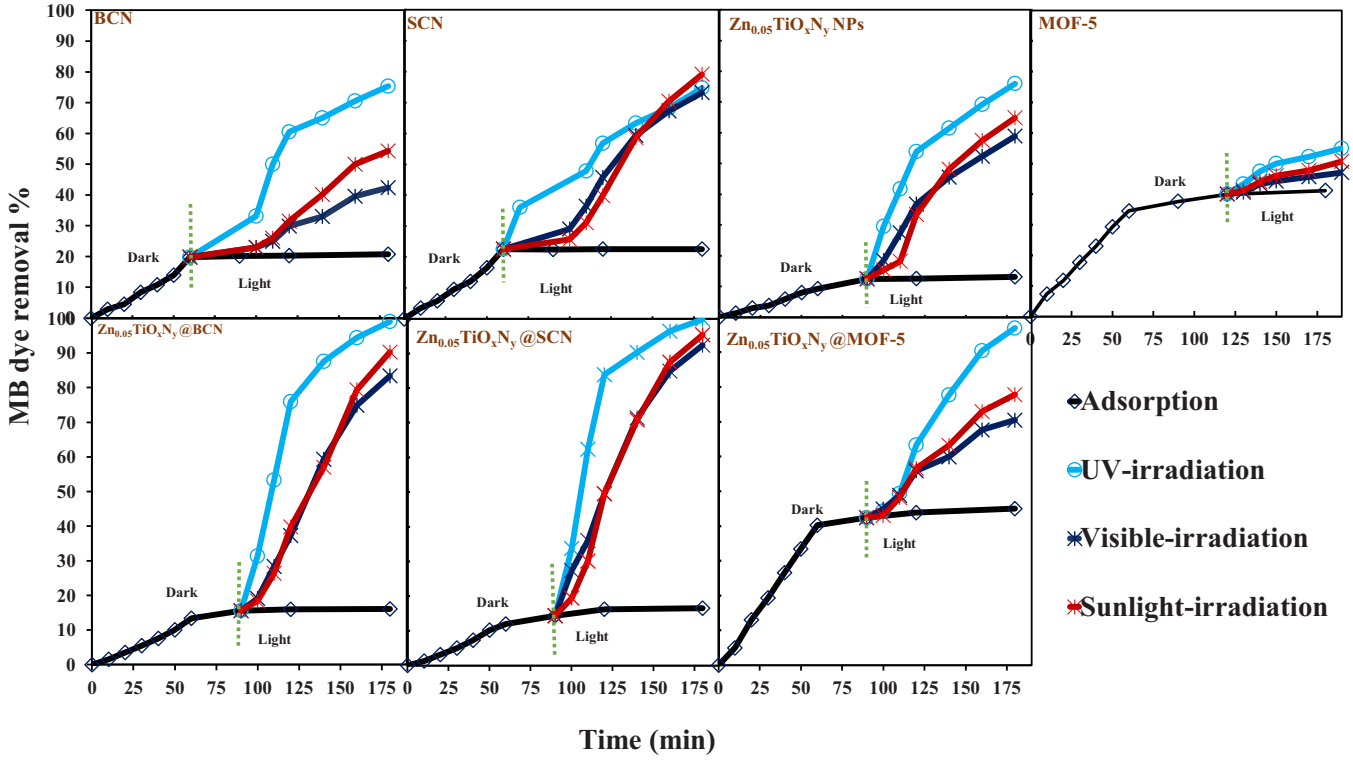

Fig. 3. Photocatalytic activities for degradation of 80 μmol/L MB dye by the photocatalysts as a function of time under different illumination sources (UV, visible, and sunlight) compared to their corresponding adsorption profiles (in the dark).

removal efficiencies of MB dye with P25 TiO_2 were 1.75%, 92.7%, and 8.9% under dark, UV, and visible light, while those of $Zn_{0.05}TiO_xN_y$ NPs were 12.4%, 75.9%, and 58.9%, respectively (Fig. S6). The above results indicated that the hybrid photocatalysts have outstanding catalytic performances towards dye decomposition under all light sources compared to the original materials. Further, the doping of TiO_2 lattice with Zn/N-atoms ($Zn_{0.05}TiO_xN_y$) is an effective approach to promoting visible/solar-driven photocatalysis, compatible with decreasing energy consumption during treatment operation.

Based on these data, the QE values (Eq. 4) were computed to be in the range of 0.56–0.49% for $Zn_{0.05}TiO_xN_y$@SCN, 0.55–0.46% for $Zn_{0.05}TiO_xN_y$@BCN, and 0.54–0.38% for $Zn_{0.05}TiO_xN_y$@MOF-5 under UV–visible light sources. The lower photocatalytic activities (e.g., QE) under visible light could be attributed to the lower photon energy/irradiance of visible light (0.103 W cm^{-2}) as compared to UV (0.239 W cm^{-2}) light source. To better understand the crucial role of the light source on the photocatalytic process, the photonic efficiency (ζ(%)) of the developed hybrid photocatalysts was estimated (Eq. 5).

$$\zeta(\%) = \Delta MB \times \Delta X_t^{-1} \times V \times E_m A \times I_0 \times 100 \quad (5)$$

Herein, ΔMB is the total moles of degraded MB dye molecules per unit volume (mol L^{-1}), ΔX_t is the irradiation time per second (s), V (L) is the volume of treated solution, I_0 (W m^{-2}) is the incident photon flux, E_m (W s mol^{-1}) is the mean energy of 1 mol photons emitted from irradiation light sources in this study, and A (m^2) is the surface area of utilized photoreactor.

The estimated photonic efficiencies (ζ%) of all developed materials were decreased with decreasing light photon flux: UV (4.74–8.33%) > sunlight (2.83–5.09%) > visible (2.04–4.45%) light sources. Among all hybrid photocatalysts, $Zn_{0.05}TiO_xN_y$@SCN had the highest ζ% values under all light sources, with 1.32–2.3-fold higher than the photonic efficiencies of pristine materials. Specifically, the computed ζ% values of hybrid photocatalysts ranked in the order of $Zn_{0.05}TiO_xN_y$ @SCN (ζ% = 8.33%, 4.45%, and 5.09%) > $Zn_{0.05}TiO_xN_y$@BCN (ζ% = 8.27%, 4.01%, and 4.82%) > $Zn_{0.05}TiO_xN_y$@MOF-5 (ζ% = 8.17%, 3.39%, and 4.15%) when using UV, visible, and sunlight sources, respectively. The high photonic efficiency of hybrid photocatalyst under sunlight (relative to visible irradiation) is reasonable due to high UV photon energy (≈5%) in the solar spectrum. This indicates the high capacity of prepared photocatalysts to absorb the UV/visible spectra in sunlight during practical photocatalytic treatment of wastewater.

Based on the above data, the superior photocatalytic activity of $Zn_{0.05}TiO_xN_y$@SCN is consistent with its optical properties in Section 3.1.3, supporting the facilitated e^-/h^+ generation/transfer mechanism between the two semiconducting materials (e.g., successful band-engineering concept) (Song et al., 2018). Besides, the enhanced adsorption performances of MOF-5 and $Zn_{0.05}TiO_xN_y$@MOF-5 could be attributed to their larger mesoporous ordering and higher surface area-to-pore volume relative to other materials (Table 1). These unique textural features of MOF-based materials could accelerate the adsorption of MB molecules (13.8−14.47 Å length × 9.5 Å width) via surface interaction and pore-diffusion mechanisms. Although $Zn_{0.05}TiO_xN_y$@MOF-5 exhibited the highest adsorption performance for MB dye, its lower photocatalytic performances (relative to SCN and $Zn_{0.05}TiO_xN_y$@SCN) may be explained based on: (i) the kinetic instability of MOF-5 in the aqueous system (collapse of the framework structure), (ii) the affinity of MOF-5 to absorb only the UV spectrum, and/or (iii) the low photon energy absorption on the surface active sites due to the high amount of adsorbed MB molecules per unit surface area on the photocatalyst surface. Accordingly, the decrease in the freely available active sites leads to a reduction of the quantum efficiency and hamper the photo-generation of radical species, which, in turn, decreased the photo-discoloration of MB dye molecules (Xu et al., 2015). On a comparative note, the high photo-activities of $Zn_{0.05}TiO_xN_y$@MOF-5 (relative to pure MOF-5, Fig. 3) is attributed mainly to the high photonic response of doped $Zn_{0.05}TiO_xN_y$ NPs (ζ% of 6.33% and 3.46% under UV and sunlight, respectively) and the MOF-5 photosensitization (i.e., adsorbed MB dye acted as a photosensitizer) (Yuan et al., 2015; Wen et al., 2017). Upon light irradiation, the adsorbed MB dye molecules are excited, followed by fast migration of photogenerated electrons from excited dye to the reactive centers (e.g., Zn_4O nodes of MOF-5 and Ti-O-Zn lattice of $Zn_{0.05}TiO_xN_y$) within $Zn_{0.05}TiO_xN_y$@MOF-5 via ligand-to-metal and metal-to-metal charge transfer mechanisms (Younis et al., 2020). The improved redox half-reactions at these catalytic centers (i.e., due to the effective e^-/h^+ separation/transfer processes) could subsequently accelerate photocatalytic activity towards the enhanced generation of ROS radicals for dye degradation.

3.2.2. *Effect of time: kinetic analysis*

The adsorption/photocatalytic degradation data of MB dyes onto the prepared photocatalysts as a function of contact time were analyzed by different kinetic models (ESI: Table S1) to understand better the synergistic effect of adsorption-photocatalysis and adsorption mechanism during the treatment process (Younis et al., 2016; El-Maghrabi et al., 2017; El-Fawal et al., 2020).

Based on the adsorption kinetic dataset in Table S2 (ESI), the nonlinear mixed first- and second-order kinetic equation (MOE, $R^2 \geq 0.99$) provided the best fit for MB dye adsorption onto all photocatalysts, with the lowest average relative error (ARE%) between the predicted and the experimental adsorption capacity vs. contact time (ARE ≤ 0.08%, Fig. S7). Kinetic fits to MOE equation indicates that the adsorption of MB dye onto all photocatalysts followed a complex physicochemical interaction mechanism (Bakhtiari and Azizian, 2015). According to the pore-diffusion kinetic curves (Fig. S8: ESI), the entire physicochemical adsorption process of MB dye onto all developed materials involves two stages: (i) a fast external mass transfer from the liquid phase to adsorbent surface sites (i.e., surface interactions) at the initial sorption stage (1–50 min: exponential phase), followed by (ii) a pore-diffusion mechanism with longer contact time (after 50–90 min: semi-equilibrium phase) (Albadarin et al., 2017). In the initial sorption stage, the adsorption interactions on the photocatalyst surfaces can include π-π stacking, van der Waals, or hydrophobic bonding with supporting materials (MOF-5 or carbon nitrides) and electrostatic (or Lewis acid/base) interactions with surface-active sites (e.g., $Zn_{0.05}TiO_xN_y$ (Zn-O and N-Ti-O), COOH (BDC linker), N–$(C)_3$, C–N–C, or N–C=S sites).

According to the Langmuir-Hinshelwood model, the photocatalytic kinetic rates (k_{photo}: min^{-1}) for MB dye onto the photocatalysts were determined based on the linear relationship between $-Ln\ (C_o/C_t)$ versus time (t, min) at different light sources (UV, visible, and sunlight: Fig. S9 and Table S3 for details) (El-Maghrabi et al., 2017). The determined adsorption vs. photocatalytic kinetic rates (k_{ads} vs. k_{photo}) of photocatalysts against MB dye removal were compared across varying light sources, as presented in Fig. 4(a). As seen in Fig. 4(a), all the prepared photocatalysts possess higher kinetic rates for MB dye adsorption than photodegradation, indicating the synergistic role of adsorption on the enhanced photocatalytic degradation process. Only $Zn_{0.05}TiO_xN_y$@SCN demonstrated a higher UV-driven photodegradation rate for MB dye than that of adsorption rate, indicating its superior activity to promote fast reactive adsorption/photocatalytic degradation of MB dye during treatment under UV light.

Under dark conditions (Fig. 4(a)), both $Zn_{0.05}TiO_xN_y$@MOF-5 and MOF-5 demonstrated the highest adsorption rates for MB dye, with k_{ads} values of 6.93 and 7.06 ($\times 10^{-2}$ min^{-1}), respectively. However, $Zn_{0.05}TiO_xN_y$@MOF-5 exhibited a faster initial rate for MB dye adsorption (h_0 = 2.75 μmol g^{-1} min^{-1}) than MOF-5 (h_0 = 2.66 μmol g^{-1} min^{-1}) within the first 50 min of the adsorption process (Table S2). These kinetic results could be attributed to the high porosity (large cage-cavity) and large surface area of MOF-5 (Table 1), which play a key role in decreasing mass transfer resistance and improving the adsorption diffusion mechanism (Abd El Salam et al., 2017). At the initial sorption

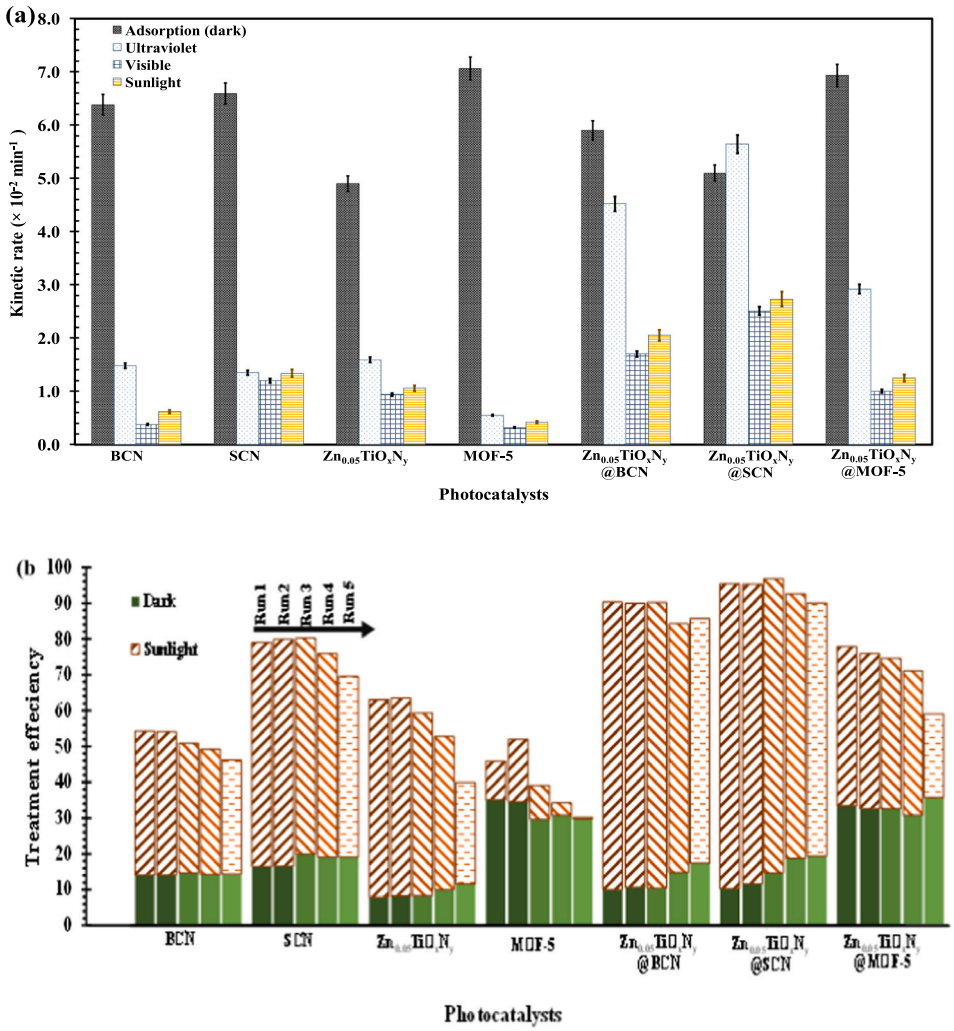

Fig. 4. Evaluation of the photocatalytic/adsorption performance of the prepared photocatalysts under different light sources: (a) adsorption/photocatalytic kinetic rates for MB dye (80 μmol/L) and (b) performance stability (5 cycles) during the treatment of real industrial wastewater.

step, the superiority of $Zn_{0.05}TiO_xN_y$@MOF-5 for MB dye uptake is mainly due to the increased number of reactive surface sites (e.g., Zn-O and N-Ti-O in $Zn_{0.05}TiO_xN_y$ NPs) available to induce reactive adsorption interaction with MB dye (h_0 value of $Zn_{0.05}TiO_xN_y$ NPs = 0.61 μmol g^{-1} min^{-1}).

Under light conditions (Fig. 4(a)), all photocatalysts showed higher photocatalytic degradation rates for MB under UV-light than those obtained under sunlight and visible irradiation. Also, all heterostructures exhibited higher photodegradation (k_{photo}) rates than the bare photocatalysts, with ranked k_{photo} values in the order of $Zn_{0.05}TiO_xN_y$@SCN > $Zn_{0.05}TiO_xN_y$@BCN > $Zn_{0.05}TiO_xN_y$@MOF-5 > $Zn_{0.05}TiO_xN_y$ ≥ SCN > BCN > MOF-5 under all light sources (Table S3: ESI). Although all supporting materials showed low photocatalytic rates, they remarkably contributed to the enhanced solar-induce photocatalytic performances of $Zn_{0.05}TiO_xN_y$ NPs ($k_{photo} \approx 1.06 \times 10^{-2}$ min^{-1}) through the formation of the hybrid heterostructures. The determined k_{photo} values of MB dye were 2.73, 2.05, and 1.25 ($\times 10^{-2}$ min^{-1}) for $Zn_{0.05}TiO_xN_y$@SCN, $Zn_{0.05}TiO_xN_y$@BCN, and $Zn_{0.05}TiO_xN_y$@MOF-5, respectively, under sunlight (Table S3). In particular, the photocatalytic (k_{photo}) rates of $Zn_{0.05}TiO_xN_y$@SCN (as a superior photocatalyst) against MB dye were 5.64, 2.51, and 2.73×10^{-2} min^{-1} under UV, visible, and sunlight, respectively. The improved photocatalytic activities of hybrid photocatalysts (relative to pristine materials) could be attributed to the accelerated vectorial transfer of photogenerated e^-/h^+ from one semiconductor to the other (e.g., interparticle electron-jump) upon illumination/excitation of their energy bandgaps (Table 1) in the heterostructures (Karunakaran et al., 2010). The accelerated charge transfer mechanism in the heterostructures could enhance the generation of ROS radicals that induce non-selective oxidation reactions with organic/microbial contaminants in the aqueous solution (as discussed later in Section 3.4).

3.3. Micobiocide activities under dark/visible light conditions

As well-known, a large number of microbes (e.g., bacterial, fungal, and yeast strains) occur in the ecosystem due to the continued discharge of untreated industrial effluents (e.g., textile wastewater) into water bodies (Prabha et al., 2017). Apart from microbes of natural origin, various microbial pathogens (e.g., *E. coli*, *S. aureus*, *Bacillus* spp., *Lactobacillus* spp., *Acinetobacter* spp., *Aeromonas* spp., and other microbes) are also reported in textile industrial wastewater depending on the treatment plant and effluent characteristics (e.g., colorants content, surfactants, dyestuff/chemical load, salinity, etc.) (Prabha et al., 2017; Buthelezi et al., 2012; Ali et al., 2009). In that context, the photo-biocidal activity of the prepared photocatalysts toward microbial inactivation was investigated to verify further their applicability for the effective treatment of textile wastewater contaminants (e.g., organic and microbial pollutants).

3.3.1. Antimicrobial activities

The antimicrobial efficiencies of pristine and hybrid photocatalysts towards the three microbial pathogens (e.g., *E. coli*, *S. aureus, and C. albicans)* in synthetic wastewater solution under dark and visible light are given in Fig. S10 (ESI). In the absence of photocatalysts (negative control), the reduction in the viable cell counts by photolysis was in the range of 1.3–4.6%, indicating the negligible effect of visible light on microbial cell viability. The photolysis results are consistent with the used visible light source, which does not emit UV-C radiation (i.e., no bactericidal illumination). During the antimicrobial experimental study, it was found that the microbiocidal (disinfection) activities of pure and heterostructured materials were dependent on the types of microbial strain and light sources. In particular, all photocatalysts displayed higher microbiocidal activity against bacterial strains (*E. coli* and *S. aureus*) than for *C. albicans* yeast strain under dark/visible light conditions. Among all photocatalysts, $Zn_{0.05}TiO_xN_y$@MOF-5 exhibited the highest microbiocidal activity for the three microbes in dark/visible-light conditions (Fig. S10 (a–b)).

Under dark conditions (Fig. S10(a)), $Zn_{0.05}TiO_xN_y$ NPs and $Zn_{0.05}TiO_xN_y$@BCN photocatalysts exhibited excellent antimicrobial efficiency (93–97%) for bacterial cells (*E. coli* and *S. aureus*), which was two times higher than that recorded against yeast cells (*C. albicans*: 49.4–57.8%). Also, the antimicrobial efficiencies of $Zn_{0.05}TiO_xN_y$@SCN and $Zn_{0.05}TiO_xN_y$@MOF-5 against *C. albicans* were 3.4–1.6-time higher than SCN and MOF-5, respectively. These results indicate the contribution of $Zn_{0.05}TiO_xN_y$ NPs in the improved microbiocidal activity of supporting materials. Under visible irradiation (Fig. S10 (b)), all photocatalysts' photo-biocidal efficiencies against the three microbes dramatically increased, as confirmed by computed photonic detoxification efficiency (MPE) in Table 2. Specifically, MOF-5, $Zn_{0.05}TiO_xN_y$ NPs, and $Zn_{0.05}TiO_xN_y$@MOF-5 have the highest ability to achieve complete inhibition of the three microbial growth under visible light, with photo-biocidal % in the range of 91–99.3%, 96.7–97.8%, and 97–99.5%, respectively (Fig. S10 (b)). Both BCN and $Zn_{0.05}TiO_xN_y$@BCN have also comparatively higher photo-biocidal % against bacterial strains (92.1–99.3%) than yeast (72–90%). However, SCN and $Zn_{0.05}TiO_xN_y$@SCN showed higher photo-biocidal % against *E. coli* and *C. albicans* (90–98%), whereas *S. aureus* showed slightly higher resistance (57.6%) against photoactivity.

3.3.2. Kinetics of biocidal activities

The Chick–Watson kinetic model (ESI: Table S1) was adopted to determine the rate of disinfection (k_m: h^{-1}) by the photocatalysts under dark and light conditions, as listed in Table 2. Photonic detoxification efficiency (MPE) was also calculated to quantify the photocatalysts' disinfection performance at constant irradiation flux (Table 2).

As can be seen in Table 2, all heterostructured materials exhibited superior disinfection rates than those obtained by pure $Zn_{0.05}TiO_xN_y$ photocatalysts due to the faster recombination of e^-/h^+ pairs during photocatalysis. Specifically, the calculated disinfection rate for $Zn_{0.05}TiO_xN_y$@MOF-5 outperformed all other photocatalysts toward the three microbial strains, with a higher rate under visible light (k_m 0.148–0.112 h^{-1}) relative to dark conditions (k_m 0.015–0.077 h^{-1}, Table 2). The calculated MPE values also confirmed that $Zn_{0.05}TiO_xN_y$@MOF-5 is far superior for the microbial disinfection process (MPE of 1.48–1.69 mCFU/Einstein) than pure $Zn_{0.05}TiO_xN_y$ NPs (MPE of 1.08–1.14 mCFU/Einstein). Pure MOF-5 also showed slightly better antimicrobial performances for *E. coli* and *S. aureus* (MPE of 1.03–1.08 mCFU/Einstein) than *C. albicans* (MPE of 0.83 mCFU/Einstein). On the other hand, $Zn_{0.05}TiO_xN_y$@MOF-5 and $Zn_{0.05}TiO_xN_y$@SCN exhibited the highest disinfection performances toward *C. albicans* (MPE of 1.48 mCFU/Einstein) among all photocatalysts. The higher disinfection rates by $Zn_{0.05}TiO_xN_y$@MOF-5 are expected to be associated with its high specific area-to-pore volume and photocatalytic activity, particularly surface plasmonic resonance (SPR) caused by synergism in the photon response within the heterostructure (Ma et al., 2016; Thakare and Ramteke, 2017). Furthermore, the enhanced disinfection rates under visible light may be attributed to the contribution of both cytotoxicity and photo-biocidal activities by the hybrid photocatalyst that leads to the microbial cell's membrane rupture, followed by oxidative damage of intercellular component (Nair et al., 2011). Nevertheless, the kinetic results confirmed the dominant role of the photo-biocidal effect for the microbial disinfection process in the dark compared to the biocidal effect (direct cytotoxicity reaction) (Table 2). In this case, the heterojunction between $Zn_{0.05}TiO_xN_y$ NPs and MOF-5 and/or C_3N_4 supports accelerated the photogeneration of e^-/h^+ active sites with a lower recombination rate during photocatalysis under visible irradiation (as discussed later in Section 3.6). Such a high photonic response enhanced the photo-induced photocatalytic generation of reactive oxygen species (ROS: such as superoxide ($^{-\bullet}O_2$) and hydroxyl (•OH) radicals)) in the system. These ROS radicals promoted all photocatalysts' microbiocidal activity via accelerating oxidative damage to microbial cell membranes and their intracellular components (i.e., cellular apoptosis) (Thakare and Ramteke, 2017; Jaffari et al., 2020).

3.4. Case-study application and reusability study

The above bench-scale experimental data demonstrated the successful application of the prepared photocatalysts in treating synthetic wastewater contaminated with MB dye and bacteria/yeast pathogens

Table 2
Kinetics rates (h^{-1}) and MPE (mCFU/Einstein) values for the photo-biocidal activities of the synthesized photocatalysts towards three microbial pathogens (*E. coli, S. aureus,* and *C. albicans*).

MPE	Light source	C–W kinetic rate constant (k_m, h^{-1})			MPE (mCFU/Einstein)[a]		
		E.coli	*S. aureus*	*C. albicans*	*E.coli*	*S. aureus*	*C. albicans*
BCN	Dark	0.021	0.027	0.015	NA	NA	NA
	Visible	0.073	0.089	0.097	1.39	1.32	1.09
SCN	Dark	0.019	0.015	0.001	NA	NA	NA
	Visible	0.072	0.052	0.095	1.38	1.17	1.07
MOF-5	Dark	0.017	0.019	0.003	NA	NA	NA
	Visible	0.102	0.138	0.099	1.03	1.08	0.83
$Zn_{0.05}TiO_xN_y$	Dark	0.023	0.028	0.011	NA	NA	NA
	Visible	0.119	0.112	0.113	1.12	1.08	1.14
$Zn_{0.05}TiO_xN_y$@SCN	Dark	0.026	0.029	0.003	NA	NA	NA
	Visible	0.127	0.022	0.105	1.49	0.94	1.48
$Zn_{0.05}TiO_xN_y$@BCN	Dark	0.023	0.076	0.014	NA	NA	NA
	Visible	0.104	0.127	0.086	1.46	1.58	0.91
$Zn_{0.05}TiO_xN_y$@MOF-5	Dark	0.031	0.077	0.015	NA	NA	NA
	Visible	0.148	0.145	0.112	1.69	1.62	1.48

[a] Quantifying the photonic efficiency of the prepared photocatalysts towards microbial inactivation, as defined by MPE (mCFU/Einstein), where the mCFU means "million colony-forming units".

under dark/light conditions. Thus, it is crucial to confirm the prepared photocatalysts' applicability for the effective treatment of real industrial wastewater effluents from a practical standpoint. Accordingly, a series of experimental tests were carried out to evaluate the adsorption/photocatalytic activities (up to five reusability cycles) towards treating real wastewater collected from the textile industry in Egypt under dark and light (UV, visible, sunlight) conditions. In this work, the collected textile effluent had initial pH, TDS, COD, and BOD_5 values of 6.43, 1248 mg/L, 2130 mg/L, and 572 mg/L, respectively. Note that the values of COD and BOD_5 (i.e., referring to persistent and biodegradable organic contaminants, respectively) were used as standard metrics in all industrial treatment plants to evaluate wastewater quality before disposal. In this respect, the calculated BOD_5/COD ratio of the collected wastewater effluent was 0.27. As the BOD_5/COD ratio is an indicator of organic biodegradability (e.g., (persistent) $0.4 > BOD_5/COD$ ratio > 0.5 (biodegradable)), the collected wastewater can thus belong to non-biodegradable effluent (Ghobashy et al., 2018; Deogaonkar et al., 2019). These results indicate the high loading contents of dissolved organic compounds (dyestuff and/or chemicals) in the collected effluent resistant to biological degradation (Deogaonkar et al., 2019).

Accordingly, photocatalysts' performance for adsorption/photocatalytic treatment of real wastewater was determined based on the percentage decline in the COD values (i.e., mineralization efficiency), as listed in Table 3. The results revealed that MOF-5 and $Zn_{0.05}TiO_xN_y$@-MOF-5 exhibited superior performances for adsorption removal of COD (% reduction) by 59.9% and 62%, respectively, after 90 min in the dark. During photocatalysis under sunlight (for 90 min), the COD % reduction remarkably increased to achieve the maximum COD removal values of 84.6% and 83.1% by $Zn_{0.05}TiO_xN_y$@SCN and $Zn_{0.0}5TiO_xN_y$@MOF-5, respectively. The obtained results under sunlight irradiation were similar (or higher) compared to the ones obtained under UV (79.8–84.5%) and visible (82.0–72.2%) light sources (Table 3). These results confirmed that the prepared materials had the capacity to act as adsorbents and/or photocatalysts to continue the treatment of real wastewater under day/night conditions. Besides, the solar-induce photocatalytic process with the hetero-structured photocatalysts is sufficient to reduce the COD content to the limit established by Egyptian law (Law 48/1982) for the discharge of textile wastewater into surface water.

The adsorption/photocatalytic stability (up to 5 reuse cycles) of the prepared photocatalysts was also investigated during textile wastewater treatment under dark and sunlight conditions, as shown in Fig. 4(b). The results revealed that the hybridization of $Zn_{0.05}TiO_xN_y$ onto all supports (BCN, SCN, and MOF-5) exhibited a noticeable improvement of adsorption/photocatalytic stability over five cycles. For pristine materials, MOF-5 showed the lowest performance stability with a 94% loss after five reuse cycles relative to 21.3% for SCN, 19.8% for BCN, and 37% for $Zn_{0.05}TiO_xN_y$ (SD (σ) ± 4.7%: Fig. 4(b)). On a comparative note, the decrease in heterostructured photocatalysts' performance was in the range of $5.6 \pm 2.09\%$ for $Zn_{0.05}TiO_xN_y$@BCN, $14.8 \pm 1.27\%$ for $Zn_{0.05}TiO_xN_y$@BCN, and $19 \pm 3.22\%$ for $Zn_{0.05}TiO_xN_y$@MOF-5 after five cycles (Fig. 4(b)). The XRD analyses also confirmed the chemical stability of hetero-structured photocatalysts after five reuse cycles, as seen in Fig. S11 (ESI). It was also noted that the XRD pattern of pure MOF-5 was considerably changed after photocatalysis, indicating its poor kinetic stability. On a comparative note, $Zn_{0.05}TiO_xN_y$@MOF-5 showed no significant change in the XRD patterns before and after photocatalysis. Only the intensity of diffraction peaks was declined after reusability cycles, with the observation of some unidentified diffraction peaks.

The lower stability of the MOF-5 based photocatalysts (XRD pattern in Fig. S11, ESI) could be attributed to the interaction of water molecules with the tetrahedral Zn_4O open metal site, leading to form a more stable 6-coordinate with two H_2O molecules in the second coordination shell. The coordinated H_2O molecules are expected to displace the BDC ligand from the $[Zn_4O]^{6+}$ cluster and consequently disrupt the MOF-5 framework (collapsed structure) (Younis et al., 2020). This phenomenon provokes, in turn, the generation of labile benzene dicarboxylate (BDC^{2-}) ligand that can participate in the adsorption of heavy metal ions in the textile wastewater solution. Due to the kinetic instability of the MOF-5 framework in the aqueous medium (Younis et al., 2020), the textural and optical properties of MOF-5 could significantly change (e.g., surface area, porosity, and catalytic sites), leading to reduce its performance stability. On the other hand, the enhanced stability of $Zn_{0.05}TiO_xN_y$@MOF-5 as compared to pure MOF-5 could be attributed to the improved hydro-stability of the MOF-5 due to the hybridization with $Zn_{0.05}TiO_xN_y$ NPs. Likewise, enhanced hydro-stability of the MOF-5 framework has been reported previously by hybridization with natural clay (i.e., attapulgite) (Lu et al., 2015) and mesoporous silica (i.e., SBA-15) (Wu et al., 2013). Accordingly, the developed $Zn_{0.05}TiO_xN_y$@MOF-5 hybrid structure is expected to possess a good hydro-stability for possible application of MOF-5 based composite in adsorption/photocatalytic treatment of wastewater under dark/solar light in this study.

3.5. Photocatalytic mechanism

3.5.1. Role of photogenerated reactive species

The photocatalytic processes were also carried out in the presence and absence of radical scavengers (5 mmol) under UV irradiation for 90 min (ESI: detail procedure in Section S1.6.1) to understand the role of ROS (e.g., •OH, h^+_{VB} or e^-_{CB}, and $O_2^{\bullet-}$) generated during photocatalysis (Table 3). In this work, disodium ethylene diamine tetraacetate (EDTA-2Na), tertbutyl alcohol (TBA), and benzoquinone (BQ) were utilized as trapping agents for holes (h^+_{VB}), •OH, and electrons (e^-_{CB})/superoxide ion ($O_2^{\bullet-}$) radicals, respectively (Zheng et al., 2017). Compared to controlled experiments (Table 3), the photocatalytic activity significantly decreased in the presence of BQ (i.e., $e^-_{CB}/O_2^{\bullet-}$ capture) and TBA (capture for •OH radical), whereas the addition of EDTA-2Na promoted the oxidation of organic contents. The enhanced photocatalytic activity by EDTA-2Na addition could be attributed to the improved photo-induced charge carrier's separation by recombination of EDTA-2Na electrons with positive h^+ sites. Note that BQ has a high

Table 3
Adsorption/photodegradation reduction of COD (%) in textile wastewater effluent (Egypt) by the prepared photocatalysts (dose = 5 g/L) in the absence and presence of 5 mmol radical scavenger agents (TBA, EDTA-2Na, and BQ).

Light source (conditions)		[a]Percentage of COD reduction values (% removal)						
		BCN	SCN	$Zn_{0.05}TiO_xN_y$	MOF-5	$Zn_{0.05}TiO_xN_y$@BCN	$Zn_{0.05}TiO_xN_y$@SCN	$Zn_{0.05}TiO_xN_y$@MOF-5
Dark (adsorption)		18.9	32.4	16.0	59.9	22.6	34.3	61.9
Visible light (photocatalysis)		50.5	62.8	62.3	63.2	71.9	82.0	72.1
Sunlight (photocatalysis)		74.2	80.3	72.1	67.2	76.1	84.6	83.1
	Control (no scavengers)	53.8	60.6	56.9	71.4	64.5	79.8	84.5
	EDTA-2Na	57.4	62.3	62.3	67.0	67.7	89.9	88.3
Ultraviolet	TBA	39.5	46.5	45.8	62.2	47.4	53.5	76.4
	BQ (O_2 atmosphere)	29.7	41.8	29.1	61.9	40.2	45.2	67.6
	BQ (N_2 atmosphere)	19.4	33.6	20.0	59.9	29.4	39.8	62.6

[a] Standard deviation for error analysis (SD) ranges from ±2.4% to ±5.1% at 95% confidence level.

inherent electron affinity (≥1.8 eV), and thereby it can be used to selectively quench photogenerated electrons under N_2 atmosphere. As seen in Table 3, the photocatalytic activities for all the photocatalysts were remarkably declined by adding BQ scavenger under N_2 atmosphere than observed under the O_2 atmosphere, signifying the crucial role of photogenerated electrons (e^-_{CB}) in the photocatalytic reaction. In this case, it is suggested that the photogenerated electrons can react with dissolved oxygen in the water to generate the $O_2^{\bullet-}$ anion as the major oxidative radical (the redox potential of $O_2/O_2^{\bullet-}$ equals −0.33 eV vs. NHE) (Sin et al., 2020). In another pathway, the formed $O_2\bullet^-$ anionic radical can be protonated to generate •OH radical (as secondary reactive species) under light irradiation by a two-electron reduction

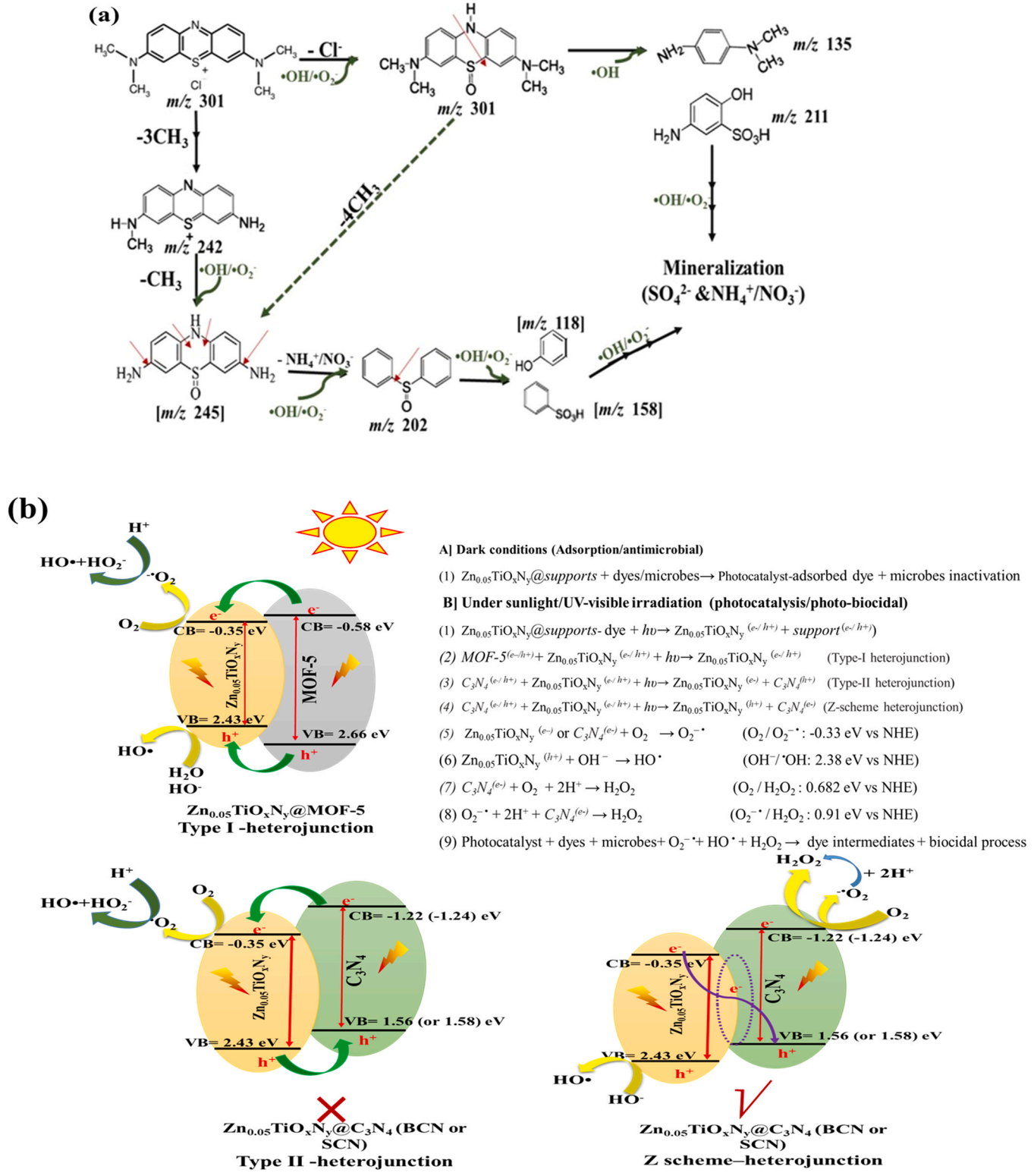

Fig. 5. The schematic diagrams for (a) the proposed photodegradation route of MB dye over $Zn_{0.05}TiO_xN_y$@SCN photocatalyst under visible irradiation for 90 min and (b) photogenerated charges transfer/separation mechanisms within the heterostructured photocatalysts under UV–visible irradiation.

transformation reaction (Das et al., 2015). Those formed ROS ($O_2\bullet^-$ and •OH) radicals are responsible for the enhanced photocatalytic activities of the heterostructured photocatalysts against dye degradation/microbial inactivation under light irradiation.

3.5.2. Detected intermediates upon MB dye photodegradation

The photocatalytic degradation pathway of MB dye (80 μmol/L) over $Zn_{0.05}TiO_xN_y$@SCN was also evaluated under visible irradiation (for 90 min) to provide more insight into the photocatalytic mechanism (Fig. 5(a)). The intermediate byproducts (organic and inorganic ions) of MB dye (molecular mass (*m/z*) 319) were identified by ultra-performance liquid chromatography-mass/mass spectroscopy (UPLC-MS/MS) and ion-exchange chromatography (IEC), as described in Section S1.6.2 (ESI). Before irradiation, the MB peak was detected at *m/z* of 284 by UPLC-MS/MS analysis, associated with cationic MB dye formation via dye's ionization (i.e., detached Cl^- ion) (Ray et al., 2017). After 30 min of photocatalysis, two peaks appeared with *m/z* of 270 and 310, corresponding to the formation of Azure C and 3,7-bis(dimethylamino)-10H-phenothiazine 5-oxide, respectively. The appearance of Azure C is attributed to the loss of three methyl groups through the breaking of terminal bonds between nitrogen and methyl groups (*e.g.*, –N–$(CH_3)_2$) (Nguyen et al., 2018). The observation of 3,7-bis(dimethylamino)-10H--phenothiazine 5-oxide indicates S=O bonds' formation, resulting from the attack of •OH/$\bullet O_2^-$ radicals onto the cationic MB dye (C–S^+=C). After 60 min of photocatalysis, the intermediate products were further degraded with the appearance of four new peaks at *m/z* values of 135, 202, 211, and 245. These peaks were attributed to the formation of dimethyl-*p*-phenylenediamine (*m/z* 135), diphenyl sulfoxide (*m/z* 202), 2-hydroxy, 5-amino, benzene sulfonic acid (*m/z* 211), and 3,7-diamino-10H-phenothiazine 5-oxide (*m/z* 245). These intermediate byproducts were formed via multiple oxidative reactions of the cationic MB ring structure (i.e., breaking of –N–C– and –C–S– bonds) by the generated oxidative •OH/$\bullet O_2^-$ radicals in the solution during photocatalysis (Ray et al., 2017). After 90 min irradiation, small peaks of low-molecular-weight organic compounds (*e.g.*, phenol (*m/z* 118) and benzene sulfonic acid (*m/z* 158)) were also detected due to the continuous oxidation of the resultant organic intermediates. The subsequent photodegradation of these byproducts produce less harmless biodegradable aliphatic organic products (e.g., methanol by oxidation of liberated CH_3 group) and mineralized inorganic ions (e.g., SO_4^{2-}, NO_3^-/NH^{4+}, and Cl^-). These mineralized inorganic ions were detected by IEC analysis at the end of the photocatalytic treatment (e.g., 72 μmol/L Cl^-, 20 μmol/L NO_3^-, 98 μmol/L NH_4^+, and 30 μmol/L SO_4^{2-}), confirming the complete mineralization of MB dye and intermediates products.

3.5.3. Photocatalytic reaction

Combining the above experimental and optical data (VB and CB position in Table 1), the photocatalytic/disinfection over all the heterostructured photocatalysts could be explained based on two mechanisms for the migration of charge carriers upon sunlight irradiation: Type-I and Type-II heterojunctions (Fig. 5(b)). In the type-I heterojunction, the excitation of $Zn_{0.05}TiO_xN_y$@MOF-5 could accelerate the interfacial transfer of photogenerated electrons/holes from MOF-5 (E_{CB} (−0.58 eV)/E_{VB} (2.66 eV)) to the $Zn_{0.05}TiO_xN_y$ NP (E_{CB} (−0.35 eV)/ E_{VB} (2.43 eV)). The accumulated electrons (e^-_{CB}) and holes (h^+_{VB}) on the CB/VB positions of $Zn_{0.05}TiO_xN_y$ have the higher redox potentials to react with O_2 and hydroxide (OH−) ions and generate $O_2^{\bullet-}$ (O_2/ $O_2^{\bullet-}$ potential (E) −0.33 eV vs. NHE) and •OH (E° of OH−/•OH = 2.38 eV vs. NHE) radicals, respectively (Lam et al., 2020).

In contrast, in the type-II heterojunction ($Zn_{0.05}TiO_xN_y$@C_3N_4: BCN or SCN), the photo-induced electrons in the CB of C_3N_4 sheets (BCN or SCN: E_{CB} of −1.24 to −1.22 eV, respectively) can be transferred to the CB of $Zn_{0.05}TiO_xN_y$. In the opposite direction, the photogenerated holes (h^+) were transferred from the VB of $Zn_{0.05}TiO_xN_y$ (high positive potential) to the VB of C_3N_4 sheets with less positive potential (Fig. 5(b)). As a result, the high potential energy of CB in $Zn_{0.05}TiO_xN_y$ can accelerate the generation of $O_2^{\bullet-}$ radical (as major ROS oxidative species) as a result of interaction between the accumulated e^-_{CB} and adsorbed O_2 molecules. However, the energy of the accumulated holes (h^+_{VB}) in C_3N_4 sheets was more negative than the potentials of OH^-/•OH and H_2O/•OH (E° of 2.72 eV vs. NHE), indicating their inability to oxidize OH^- or H_2O into •OH radicals (Sin et al., 2020). This mechanism conflicted with the radical scavenger data (Table 3), which confirmed the crucial roles of $O_2^{\bullet-}$ and •OH radicals on the photocatalysis process. Accordingly, it is suggested that the separation/migration of photogenerated charges in $Zn_{0.05}TiO_xN_y$@C_3N_4 heterostructures may follow Z-scheme heterojunction to retain the strong redox potentials of active species in each catalyst. In this scheme, the excited electrons in the CB of $Zn_{0.05}TiO_xN_y$ transferred to the VB of C_3N_4 sheets (i.e., recombined with positive h^+), leading to an increase in the lifetime of photogenerated e^-/h^+ pairs in $Zn_{0.05}TiO_xN_y$@C_3N_4 heterostructures. At this stage, the accumulated e^-_{CB} in C_3N_4 sheets (CB −1.22 to −1.24 eV) had the high potential to initiate spontaneous catalytic reactions to generate $O_2^{\bullet-}$ radical and H_2O_2 oxidant (Fig. 5(b)) (Sin et al., 2020). On the other hand, the VB position of $Zn_{0.05}TiO_xN_y$ can oxidize OH− ions to form •OH radicals. These formed oxidative species ($O_2\bullet^-$ and •OH radicals) ultimately promote solar-induced photodegradation of organic dyes and deactivation of microbial cells in aqueous solution.

3.6. Photocatalytic performance comparison

Table 4 lists a comparison of adsorption/photocatalytic performances of the prepared photocatalysts (relative to published photocatalysts) towards the removal of various textile dyes (e.g., MB, RhB (Rhodamine B), and MO (methyl orange)) under visible light. As seen, the computed adsorption/photocatalytic rates (k_{ads} and k_{Photo}: min^{-1}) values obtained with the prepared heterostructured photocatalysts are significantly higher than those reported for other photocatalysts for dyes removal. Within the reported photocatalysts, Ag/TiO_2, g-C_3N_4/MIL-125 (Ti), and AlZnO/G photocatalysts were found to have higher k_{Photo} values (5.15–14.5 $\times 10^{-2}$ min^{-1}) as compared with that obtained by the heterostructures in this study (k_{Photo} = 1.0–2.51 $\times 10^{-2}$ min^{-1}). This observation is likely attributed to the change in experimental conditions (e.g., the use of high light outputs (200– 300 W) for irradiation and/or low initial dye concentration (47–50 μmol/l)). The decrease in initial dye concentration could reduce solution opacity. With decreased water opacity, more photon light can migrate through a water solution to activate catalytic surface sites for enhanced generation of charge carriers (El-Fawal et al., 2020; Younis and Kim, 2020). Likewise, as the light irradiance increases, the transmission of photon light into the water increases as well. Such phenomena enhance catalyst excitation (i.e., accelerate charge carriers generation) and subsequently promote oxidative radical species' production to degrade organic dyes (as discussed earlier). More importantly, it was also found that there is a large variation in the quality (demineralized, saline, and real water) and volume/depth (from 50 to 200 mL) of dye-contaminated wastewater used in the published experimental studies. Such variation in water quality and volume (or depth) could remarkably influence the photocatalytic efficiency by affecting the penetration depth of photon in water. These results suggest that the applicability of photocatalysis for industrial wastewater treatment depends not only on the target photocatalyst's photoactivity but also on the light irradiance, water quality, and water depth. These parameters considerably influence the maximum amount of photon light that reached the catalysts' surface for excitation and initiated the photocatalytic treatment process. Accordingly, during the practical application of photocatalysis in real-fields, it is critically important to optimize these parameters via: (i) hybridizing photocatalysis with other traditional pre-treatment methods to improve water quality (e.g., reduce the water color to the minimal limits), and (ii) coupling adsorption/photocatalysis to promote and maximize treatment efficiency in light/dark conditions.

Table 4
Comparison of adsorption/photocatalytic performance of the prepared materials (in this work) with some other photocatalysts in the literature.

Sr. No.	Photocatalyst materials	Characterization		Experimental conditions				Experimental results				References
		Optical bandgap (E_g: eV)	BET (m^2/g)	Light/ power (W)	Dye/ Conc. (μmol/l)	pH/ catalyst dose (g/L)	Ads/ Photo time (min)	q_e (μmol/ g)	k_{ads} ($\times10^{-2}$ min^{-1})	k_{photo} ($\times10^{-2}$ min^{-1})	R %	
1	$Zn_{0.05}TiO_xN_y$@SCN	2.79	51	Vis/72 W	MB/80	6.5/1.0	90/90	14.38	5.1	2.51	92.4	This work
2	$Zn_{0.05}TiO_xN_y$@BCN	2.68	44	Vis/72 W	MB/80	6.5/1.0	90/90	15.53	5.9	1.70	83.5	This work
3	$Zn_{0.05}TiO_xN_y$@MOF-5	2.83	904	Vis/72 W	MB/80	6.5/1.0	90/90	42.45	6.93	1.00	70.5	This work
4	$Zn_{0.05}TiO_xN_y$	2.77	62	Vis/72 W	MB/80	6.5/1.0	90/90	12.41	4.90	0.94	58.9	This work
5	SCN	2.78	86	Vis/72 W	MB/80	6.5/1.0	90/90	22.41	6.59	1.20	73.2	This work
6	BCN	2.81	36	Vis/72 W	MB /80	6.5/1.0	90/90	20.19	6.38	0.38	42.3	This work
7	MOF-5	3.23	1291	Vis/72 W	MB/80	6.5/1.0	90/90	37.6	7.06	0.32	48.3	This work
8	P25 TiO_2 (commercial)	3.2	–	Vis/72 W	MB/80	6.5/1.0	90/90	1.4	0.39	0.11	8.9	This work
9	g-C_3N_4/MIL-125(Ti)	3.24	328	Vis/ 300 W	RhB/104	-/0.16	60/60	103.3	–	6.24	95.2	Wang et al. (2015)
10	g-C_3N_4	2.45	6.2	Vis/ 300 W	RhB/104	-/0.16	60/60	62.4	–	2.99	81.3	
11	MIL-125(Ti)	3.68	1548.3	Vis/ 300 W	RhB/104	-/0.16	60/60	8.8	–	0.26	10.1	
12	AlZnO/PANI (PAZ-2)	2.57	–	Vis/ 200 W	RhB/10	7/0.40	30/150	–	–	2.61	98.0	Mitra et al. (2017)
13	AlZnO/PANI (PAZ-2)	2.57	–	Vis/ 200 W	MO/10	7/0.40	30/150	–	–	1.77	92.5	
14	ZnO	2.92	–	Vis/ 200 W	RhB/10	7/0.40	30/150	–	–	0.08	–	
15	ZnO	2.92	–	Vis/ 200 W	MO/10	7/0.40	30/150	–	–	0.05	–	
16	AlZnO	3.03	–	Vis/ 200 W	RhB/10	7/0.40	30/150	–	–	0.32	–	
17	AlZnO	3.03	–	Vis/ 200 W	MO/10	7/0.40	30/150	–	–	0.12	–	
18	Sn doped N-TiO_2	2.82	–	Sunlight	MO/60	–/1.0	30/120	–	–	3.40	95.0	Kadam et al. (2017)
19	AlZnO	3.22	32.69	Vis/72 W	MB/50	6.5/0.5	90/60	1.097	0.005	0.18	24.9	El-Fawal et al. (2020)
20	AlZnO/PANI	3.02	24.08	Vis/72 W	MB/50	6.5/0.5	90/60	30.85	0.12	1.92	59.3	
21	AlZnO/g-C_3N_4	2.62	35.25	Vis/72 W	MB/50	6.5/0.5	90/60	30.23	0.19	2.82	92.2	
22	AlZnO/CNT	2.8	146	Vis/72 W	MB/50	6.5/0.5	90/60	56.18	0.44	3.37	71.9	
23	AlZnO/CNF	2.82	86.6	Vis/72 W	MB/50	6.5/0.5	90/60	44.81	0.33	2.26	56.5	
24	AlZnO/G	2.71	230.8	Vis/72 W	MB/50	6.5/0.5	90/60	79.89	0.82	5.15	88.3	
25	Ag/TiO_2	–	–	Vis/ 300 W	MB/47	-/0.11	40/80	–	–	14.50	97.0	Tahir et al. (2016)
26	TiO_2	–	–	Vis/ 300 W	MB/47	-/0.11	40/80	–	–	7.20	77.0	
27	Ag NPs	–	–	Vis/ 300 W	MB/47	-/0.11	40/80	–	–	5.90	35.0	
28	BiOBr/$MnFe_2O_4$-10	–	–	Vis/ 105 W	RhB/ 42	5.1/1.0	60/80	–	–	2.57	89.3	
29	$MnFe_2O_4$	1.85	–	Vis/ 105 W	RhB/ 42	5.1/1.0	60/80	–	–	0.40	24.9	Sin et al. (2020)
30	BiOBr	2.97	–	Vis/ 105 W	RhB/ 42	5.1/1.0	60/80	–	–	0.90	48.5	
31	TiO_2 (commercial)	–	–	Vis/ 105 W	RhB/ 42	5.1/1.0	60/80	–	–	0.27	17.2	

Notes: PANI = polyaniline; CNT = carbon nanotube; CNF = carbon nanofiber; G = graphene; MO = methyl orange dye; RhB = Rhodamine B dye.

4. Conclusion

Three hierarchical photo-sorbent materials were successfully synthesized by in-situ encapsulation of $Zn_{0.05}TiO_xN_y$ NPs (6–34 nm) into 2D free and sulfur-doped graphitic carbon nitride sheets and 3D cubic MOF-5 framework using a microwave-assisted method. The optical features strongly confirm the effectiveness of hetero-structured photocatalysts (E_g = 2.68–2.83 eV) to promote solar-initiated-light-responsive photocatalysis. Specifically, $Zn_{0.05}TiO_xN_y$@MOF-5 outperformed all other photocatalysts in terms of MB dye sorption (q_e of 42.5 μmol g^{-1} with k_{ads} rate of 6.9×10^{-2} min^{-1}) and antimicrobial efficiencies for *E. coli* (83%), *S. aureus* (96.5%), and *C. albicans* yeast (53.2%) under dark condition. The results of photonic detoxification efficiencies showed that the microbial inactivation was promoted with hetero-structured photocatalysts to achieve 97–99.3% inhibition growth under visible irradiation due to the vital role of photocatalysis in the disinfection process. Our study also showed effective sunlight-induced photocatalytic treatment for real textile wastewater (COD reduction by 76.1–84.6%) by all hybrid photocatalysts, with relatively stable performances up to 5 cycles. Based on the radical scavengers and MB dye photodegradation pathway, the enhanced photocatalytic activities were attributed to the formation of reactive oxidative species ($O_2^{\bullet-}$ and •OH radicals) and the separation of photogenerated e^-/h^+ charge carriers. In this respect, the photoactive supporting materials (BCN, SCN, and MOF-5) improved the photon harvesting properties in the UV–visible region. In contrast, the dopant $Zn_{0.05}TiO_xN_y$ NPs assisted e^-/h^+ charge carriers' separation via a well-aligned overlapping energy band potential structure-property (i.e., band-engineering concept). As such, this work

opens new prospects for further tuning and utilization of these heterostructured photocatalysts for advanced treatment of industrial wastewater to respond to the growing demand for clean water resources. Further studies are in course with the aim to: (i) understand the electrochemical properties and solvo/hydrothermal stability of the prepared $Zn_{0.05}TiO_xN_y$@MOF-5 versus $Zn_{0.05}TiO_xN_y$@g-C_3N_4 hybrids, and (ii) evaluate the effect of operating parameters (e.g., pH, salinity, initial pollutant concentration, and temperature) on their adsorption photocatalytic performances.

CRediT authorship contribution statement

Sherif A. Younis: Conceptualization, Experimental design, Methodology, Investigation, Materials synthesis & characterization, Wastewater treatment applications, Data analysis & curation, Writing - original draft, Writing - review & editing. **Philippe Serp:** Provided the facilities for material synthesis & characterization, Validation, Data curation, Editing & revision, Supervision. **Hussein N. Nassar:** Conceptualization, Methodology, Biocidal experimental studies, Data interpretation, Writing - review & editing.

Declaration of Conflict-of-interest

The authors declare that they have no known competing financial interests or personal relationships that could have appeared to influence the work reported in this paper.

Acknowledgment

The French and Egyptian Governments supported this work through a co-financed fellowship granted by the French Embassy in Egypt (Institut Français d'Egypte, IFE) and the Science and Technology Development Fund (STDF), funded project (IFE-STDF No. 26470). The authors are appreciative to the Egyptian Petroleum Research Institute (EPRI) Laboratories for providing the required analytical techniques used in this study. The authors are also grateful to David Neumeyer at the Centre d'Élaboration de Matériaux et d'Etudes Structurales (CEMES-CNRS) for providing the optical analysis support.

Appendix A. Abbreviation/acronym/symbol

CFU	Colony-forming units
ε_{mb}	Photonic detoxification efficiency
h_o (μmol g^{-1} min^{-1})	Initial sorption rate
HOMO	Highest Occupied Molecular Orbital
k_{ads} (min^{-1})	Adsorption kinetic rate
k_{photo} (min^{-1})	Photocatalytic kinetic rate
k_i (μmol g^{-1} $min^{-0.5}$)	Pore diffusion kinetic rates
k_m (h^{-1})	biocidal/antimicrobial kinetic rate
LMCT	Ligand-metal charge transfer
LUMO	Lowest Unoccupied Molecular Orbital
MOE	Mixed-order kinetic model
MPE (mCFU/Einstein)	Microbicide photonic efficiencies
MW	Microwave
q_e (μmol/g)	Adsorption capacity

Appendix B. Supporting information

Supplementary data associated with this article can be found in the online version at doi:10.1016/j.jhazmat.2020.124562.

References

Abd El Salam, H.M., Younis, S.A., Ali, H.R., Zaki, T., 2017. Statistical modeling and optimization of phenol adsorption from water by modified Cu3(BTC)2: Kinetic, isotherm, and thermodynamic analysis. Microporous Mesoporous Mater. 241, 210–217. https://doi.org/10.1016/j.micromeso.2016.12.010.

Albadarin, A.B., Collins, M.N., Naushad, M., Shirazian, S., Walker, G., Mangwandi, C., 2017. Activated lignin-chitosan extruded blends for efficient adsorption of methylene blue. Chem. Eng. J. 307, 264–272. https://doi.org/10.1016/j.cej.2016.08.089.

Ali, N., Hameed, A., Ahmed, S., 2009. Physicochemical characterization and bioremediation perspective of textile effluent, dyes and metals by indigenous bacteria. J. Hazard. Mater. 164, 322–328. https://doi.org/10.1016/j.jhazmat.2008.08.006.

Aoki, Y., Sakurai, M., Coh, S., Chelikowsky, J.R., Louie, S.G., Cohen, M.L., Saito, S., 2019. Insulating titanium oxynitride for visible light photocatalysis. Phys. Rev. B 99, 1–6. https://doi.org/10.1103/PhysRevB.99.075203.

Bakhtiari, N., Azizian, S., 2015. Adsorption of copper ion from aqueous solution by nanoporous MOF-5: a kinetic and equilibrium study. J. Mol. Liq. 206, 114–118.

Buthelezi, S.P., Olaniran, A.O., Pillay, B., 2012. Textile dye removal from wastewater effluents using bioflocculants produced by indigenous bacterial isolates. Molecules 17, 14260–14274. https://doi.org/10.3390/molecules171214260.

Caudillo-Flores, U., Muñoz-Batista, M.J., Luque, R., Fernández-García, M., Kubacka, A., 2019. g-C3N4/TiO2 composite catalysts for the photo-oxidation of toluene: chemical and charge handling effects. Chem. Eng. J. 378, 122228 https://doi.org/10.1016/j.cej.2019.122228.

Choi, J.Y., Kim, J., Jhung, S.H., Kim, H., Chang, J., Chae, H.K., 2006. Microwave synthesis of a porous metal-organic framework, zinc terephthalate MOF-5. Bull. Korean Chem. Soc. 27, 1523–1524. https://doi.org/10.5012/bkcs.2006.27.10.1523.

Chu, Y., Hou, J., Boyer, C., Richardson, J.J., Liang, K., Xu, J., 2018. Biomimetic synthesis of coordination network materials: recent advances in MOFs and MPNs. Appl. Mater. Today 10, 93–105. https://doi.org/10.1016/j.apmt.2017.12.009.

Das, S., Sinha, S., Suar, M., Yun, S.-I., Mishra, A., Tripathy, S.K., 2015. Solar-photocatalytic disinfection of Vibrio cholerae by using Ag@ZnO core–shell structure nanocomposites. J. Photochem. Photobiol. B Biol. 142, 68–76. https://doi.org/10.1016/j.jphotobiol.2014.10.021.

Deng, J., Wang, M., Fang, J., Song, X., Yang, Z., Yuan, Z., 2019. Synthesis of Zn-doped TiO_2 nano-particles using metal Ti and Zn as raw materials and application in quantum dot sensitized solar cells. J. Alloy. Compd. 791, 371–379. https://doi.org/10.1016/j.jallcom.2019.03.306.

Deogaonkar, S.C., Wakode, P., Rawat, K.P., 2019. Electron beam irradiation post treatment for degradation of non biodegradable contaminants in textile wastewater. Radiat. Phys. Chem. 165, 108377 https://doi.org/10.1016/j.radphyschem.2019.108377.

Dong, S., Cui, L., Zhang, W., Xia, L., Zhou, S., Russell, C.K., Fan, M., Feng, J., Sun, J., 2020. Double-shelled $ZnSnO_3$ hollow cubes for efficient photocatalytic degradation of antibiotic wastewater. Chem. Eng. J. 384, 123279 https://doi.org/10.1016/j.cej.2019.123279.

El-Fawal, E.M., Younis, S.A., Moustafa, Y.M., Serp, P., 2020. Preparation of solar-enhanced AlZnO@carbon nano-substrates for remediation of textile wastewaters. J. Environ. Sci. 92, 52–68. https://doi.org/10.1016/j.jes.2020.02.003.

El-Maghrabi, H.H., Ali, H.R., Younis, S.A., 2017. Construction of a new ternary α-MoO3–WO3/CdS solar nanophotocatalyst towards clean water and hydrogen production from artificial wastewater using optimal design methodology. RSC Adv. 7, 4409–4421. https://doi.org/10.1039/C6RA25146C.

Elshafie, M., Younis, S.A., Serp, P., Gad, E.A.M., 2020. Preparation characterization and non-isothermal decomposition kinetics of different carbon nitride sheets. Egypt. J. Pet. 29, 21–29. https://doi.org/10.1016/j.ejpe.2019.09.003.

Ertugay, N., Acar, F.N., 2017. Removal of COD and color from Direct Blue 71 azo dye wastewater by Fenton's oxidation: kinetic study. Arab. J. Chem. 10, S1158–S1163. https://doi.org/10.1016/j.arabjc.2013.02.009.

Etacheri, V., Seery, M.K., Hinder, S.J., Pillai, S.C., 2010. Highly visible light active TiO_2-xNx heterojunction photocatalysts. Chem. Mater. 22, 3843–3853. https://doi.org/10.1021/cm903260f.

Fatima, R., Afridi, M.N., Kumar, V., Lee, J., Ali, I., Kim, K.H., Kim, J.O., 2019. Photocatalytic degradation performance of various types of modified TiO2 against nitrophenols in aqueous systems. J. Clean. Prod. 231, 899–912. https://doi.org/10.1016/j.jclepro.2019.05.292.

Ferrari-Lima, A.M., De Souza, R.P., Mendes, S.S., Marques, R.G., Gimenes, M.L., Fernandes-Machado, N.R.C., 2015. Photodegradation of benzene, toluene and xylenes under visible lightapplying N-doped mixed TiO_2 and ZnO catalysts. Catal. Today 241, 40–46. https://doi.org/10.1016/j.cattod.2014.03.042.

Ghobashy, M.M., Younis, S.A., Elhady, M.A., Serp, P., 2018. Radiation induced in-situ cationic polymerization of polystyrene organogel for selective absorption of cholorophenols from petrochemical wastewater. J. Environ. Manag. 210, 307–315. https://doi.org/10.1016/j.jenvman.2018.01.018.

Grasset, F., Allegret-Maret, V., Berthebaud, D., Ababou-Girard, S., Pechev, S., 2007. Tunable optical absorption on "ZnxTixO4-3yN2y" nanosized spinel powders. J. Phys. Chem. C. 111, 7883–7888. https://doi.org/10.1021/jp0716334.

Hafizovic, J., Bjørgen, M., Olsbye, U., Dietzel, P.D.C., Bordiga, S., Prestipino, C., Lamberti, C., Lillerud, K.P., 2007. The inconsistency in adsorption properties and powder XRD data of MOF-5 is rationalized by framework interpenetration and the presence of organic and inorganic species in the nanocavities. J. Am. Chem. Soc. 129, 3612–3620. https://doi.org/10.1021/ja0675447.

Hao, X., Cui, Z., Zhou, J., Wang, Y., Hu, Y., Wang, Y., Zou, Z., 2018. Architecture of high efficient zinc vacancy mediated Z-scheme photocatalyst from metal-organic frameworks. Nano Energy 52, 105–116. https://doi.org/10.1016/j.nanoen.2018.07.043.

Jaffari, Z.H., Lam, S.M., Sin, J.C., Zeng, H., Mohamed, A.R., 2020. Magnetically recoverable Pd-loaded BiFeO3 microcomposite with enhanced visible light photocatalytic performance for pollutant, bacterial and fungal elimination. Sep. Purif. Technol. 236, 116195 https://doi.org/10.1016/j.seppur.2019.116195.

Jiang, D., Xu, P., Wang, H., Zeng, G., Huang, D., Chen, M., Lai, C., Zhang, C., Wan, J., Xue, W., 2018. Strategies to improve metal organic frameworks photocatalyst's performance for degradation of organic pollutants. Coord. Chem. Rev. 376, 449–466. https://doi.org/10.1016/j.ccr.2018.08.005.

Kadam, A., Dhabbe, R., Shin, D.-S., Garadkar, K., Park, J., 2017. Sunlight driven high photocatalytic activity of Sn doped N-TiO2 nanoparticles synthesized by a microwave assisted method. Ceram. Int. 43, 5164–5172. https://doi.org/10.1016/j.ceramint.2017.01.039.

Karunakaran, C., Dhanalakshmi, R., Gomathisankar, P., Manikandan, G., 2010. Enhanced phenol-photodegradation by particulate semiconductor mixtures: interparticle electron-jump. J. Hazard. Mater. 176, 799–806. https://doi.org/10.1016/j.jhazmat.2009.11.105.

Ke, L., Li, P., Wu, X., Jiang, S., Luo, M., Liu, Y., Le, Z., Sun, C., Song, S., 2017. Graphene-like sulfur-doped g-C_3N_4 for photocatalytic reduction elimination of UO_2^{2+} under visible Light. Appl. Catal. B Environ. 205, 319–326. https://doi.org/10.1016/j.apsusc.2017.06.065.

Lam, S.M., Sin, J.C., Lin, H., Li, H., Lim, J.W., Zeng, H., 2020. A Z-scheme WO_3 loaded-hexagonal rod-like ZnO/Zn photocatalytic fuel cell for chemical energy recuperation from food wastewater treatment. Appl. Surf. Sci. 514, 145945 https://doi.org/10.1016/j.apsusc.2020.145945.

Liu, M., Zhang, D., Han, J., Liu, C., Ding, Y., Wang, Z., Wang, A., 2020. Adsorption enhanced photocatalytic degradation sulfadiazine antibiotic using porous carbon nitride nanosheets with carbon vacancies. Chem. Eng. J. 382, 123017 https://doi.org/10.1016/j.cej.2019.123017.

Li, W., Mu, B., Yang, Y., 2019. Feasibility of industrial-scale treatment of dye wastewater via bio-adsorption technology. Bioresour. Technol. 277, 157–170. https://doi.org/10.1016/j.biortech.2019.01.002.

Lu, L., Li, X.Y., Liu, X.Q., Wang, Z.M., Sun, L.B., 2015. Enhancing the hydrostability and catalytic performance of metal-organic frameworks by hybridizing with attapulgite, a natural clay. J. Mater. Chem. A. 3, 6998–7005. https://doi.org/10.1039/c5ta00959f.

Martín-Betancor, K., Aguado, S., Rodea-Palomares, I., Tamayo-Belda, M., Leganés, F., Rosal, R., Fernández-Piñas, F., 2017. Co, Zn and Ag-MOFs evaluation as biocidal materials towards photosynthetic organisms. Sci. Total Environ. 595, 547–555. https://doi.org/10.1016/j.scitotenv.2017.03.250.

Ma, S., Zhan, S., Jia, Y., Shi, Q., Zhou, Q., 2016. Enhanced disinfection application of Ag-modified g-C_3N_4 composite under visible light. Appl. Catal. B Environ. 186, 77–87. https://doi.org/10.1016/j.apcatb.2015.12.051.

Mirsoleimani-azizi, S.M., Setoodeh, P., Zeinali, S., Rahimpour, M.R., 2018. Tetracycline antibiotic removal from aqueous solutions by MOF-5: adsorption isotherm, kinetic and thermodynamic studies. J. Environ. Chem. Eng. 6, 6118–6130.

Mitra, M., Ghosh, A., Mondal, A., Kargupta, K., Ganguly, S., Banerjee, D., 2017. Facile synthesis of aluminium doped zinc oxide-polyaniline hybrids for photoluminescence and enhanced visible-light assisted photo-degradation of organic contaminants. Appl. Surf. Sci. 402, 418–428. https://doi.org/10.1016/j.apsusc.2017.01.072.

Nair, R.G., Roy, J.K., Samdarshi, S.K., Mukherjee, A.K., 2011. Enhanced visible light photocatalytic disinfection of gram negative, pathogenic Escherichia coli bacteria with Ag/TiV oxide nanoparticles. Colloids Surf. B Biointerfaces 86, 7–13. https://doi.org/10.1016/j.colsurfb.2011.03.011.

Nguyen, C.H., Fu, C.C., Juang, R.S., 2018. Degradation of methylene blue and methyl orange by palladium-doped TiO2 photocatalysis for water reuse: efficiency and degradation pathways. J. Clean. Prod. 202, 413–427. https://doi.org/10.1016/j.jclepro.2018.08.110.

Oh, W.-D., Lok, L.-W., Veksha, A., Giannis, A., Lim, T.-T., 2018. Enhanced photocatalytic degradation of bisphenol A with Ag-decorated S-doped g-C 3 N 4 under solar irradiation: performance and mechanistic studies. Chem. Eng. J. 333, 739–749. https://doi.org/10.1016/j.cej.2017.09.182.

Pattnaik, P., Dangayach, G.S., Bhardwaj, A.K., 2018. A review on the sustainability of textile industries wastewater with and without treatment methodologies. Rev. Environ. Health 33, 163–203.

Pérez-larios, A., Lopez, R., Hernández-gordillo, A., Tzompantzi, F., Gómez, R., Torres-guerra, L.M., 2012. Improved hydrogen production from water splitting using TiO_2 – ZnO mixed oxides photocatalysts. Fuel 100, 139–143. https://doi.org/10.1016/j.fuel.2012.02.026.

Prabha, S., Gogoi, A., Mazumder, P., Ramanathan, A., Kumar, M., 2017. Assessment of the impact of textile effluents on microbial diversity in Tirupur district, Tamil Nadu. Appl. Water Sci. 7, 2267–2277. https://doi.org/10.1007/s13201-016-0394-3.

Qiao, L., Xie, F., Xie, M., Gong, C., Wang, W., Gao, J., 2016. Characterization and photoelectrochemical performance of Zn-doped TiO2 films by sol–gel method. Trans. Nonferrous Met. Soc. China 26, 2109–2116. https://doi.org/10.1016/S1003-6326(16)64325-X.

Ray, S.K., Dhakal, D., Kshetri, Y.K., Lee, S.W., 2017. Cu-α-NiMoO4 photocatalyst for degradation of methylene blue with pathways and antibacterial performance. J. Photochem. Photobiol. A Chem. 348, 18–32. https://doi.org/10.1016/j.jphotochem.2017.08.004.

Reddy, C.V., Reddy, K.R., Harish, V.V.N., Shim, J., Shankar, M.V., Shetti, N.P., Aminabhavi, T.M., 2020. Metal-organic frameworks (MOFs)-based efficient heterogeneous photocatalysts: synthesis, properties and its applications in photocatalytic hydrogen generation, CO_2 reduction and photodegradation of organic dyes. Int. J. Hydrog. Energy 45, 7656–7679. https://doi.org/10.1016/j.ijhydene.2019.02.144.

Sahoo, S.K., Tripathy, M., Hota, G., 2019. In-situ functionalization of GO sheets with AlOOH-FeOOH composite nanorods: an eco-friendly nanoadsorbent for removal of toxic arsenate ions from water. J. Environ. Chem. Eng. 7, 103357.

Sin, J.C., Lam, S.M., Zeng, H., Lin, H., Li, H., Kugan Kumaresan, A., Mohamed, A.R., Lim, J.W., 2020. Z-scheme heterojunction nanocomposite fabricated by decorating magnetic MnFe2O4 nanoparticles on BiOBr nanosheets for enhanced visible light photocatalytic degradation of 2,4-dichlorophenoxyacetic acid and Rhodamine B. Sep. Purif. Technol. 250, 117186 https://doi.org/10.1016/j.seppur.2020.117186.

Song, X., Yang, Q., Yin, M., Tang, D., Zhou, L., 2018. Highly efficient pollutant removal of graphitic carbon nitride by the synergistic effect of adsorption and photocatalytic degradation. RSC Adv. 8, 7260–7268. https://doi.org/10.1039/c7ra11467b.

Tahir, K., Ahmad, A., Li, B., Nazir, S., Khan, A.U., Nasir, T., Khan, Z.U.H., Naz, R., Raza, M., 2016. Visible light photo catalytic inactivation of bacteria and photo degradation of methylene blue with Ag/TiO_2 nanocomposite prepared by a novel method. J. Photochem. Photobiol. B Biol. 162, 189–198. https://doi.org/10.1016/j.jphotobiol.2016.06.039.

Thakare, S.R., Ramteke, S.M., 2017. Fast and regenerative photocatalyst material for the disinfection of E. coli from water: silver nano particle anchor on MOF-5. Catal. Commun. 102, 21–25. https://doi.org/10.1016/j.catcom.2017.06.008.

Tian, S., Xu, S., Liu, J., He, C., Xiong, Y., Feng, P., 2019. Highly efficient removal of both cationic and anionic dyes from wastewater with a water-stable and eco-friendly Fe-MOF via host-guest encapsulation. J. Clean. Prod. 239, 117767 https://doi.org/10.1016/j.jclepro.2019.117767.

Wang, H., Qiu, X., Liu, W., Yang, D., 2017. Facile preparation of well-combined lignin-based carbon/ZnO hybrid composite with excellent photocatalytic activity. Appl. Surf. Sci. 426, 206–216. https://doi.org/10.1016/j.apsusc.2017.07.112.

Wang, H., Yuan, X., Wu, Y., Zeng, G., Chen, X., Leng, L., Li, H., 2015. Synthesis and applications of novel graphitic carbon nitride/metal-organic frameworks mesoporous photocatalyst for dyes removal. Appl. Catal. B, Environ. 174–175, 445–454. https://doi.org/10.1016/j.apcatb.2015.03.037.

Wen, M., Mori, K., Kuwahara, Y., An, T., Yamashita, H., 2017. Design and architecture of metal organic frameworks for visible light enhanced hydrogen production. Appl. Catal. B Environ. 218, 555–569. https://doi.org/10.1016/j.apcatb.2017.06.082.

Wu, C.M., Rathi, M., Ahrenkiel, S.P., Koodali, R.T., Wang, Z., 2013. Facile synthesis of MOF-5 confined in SBA-15 hybrid material with enhanced hydrostability. Chem. Commun. 49, 1223–1225. https://doi.org/10.1039/c2cc38366g.

Xu, H.Y., Wu, L.C., Zhao, H., Jin, L.G., Qi, S.Y., 2015. Synergic effect between adsorption and photocatalysis of metal-free g-C_3N_4 derived from different precursors. PLoS One 10, 1–20. https://doi.org/10.1371/journal.pone.0142616.

Yahya, N., Aziz, F., Jamaludin, N.A., Mutalib, M.A., Ismail, A.F., Salleh, W.N.W., Jaafar, J., Yusof, N., Ludin, N.A., 2018. A review of integrated photocatalyst adsorbents for wastewater treatment. J. Environ. Chem. Eng. 6, 7411–7425. https://doi.org/10.1016/j.jece.2018.06.051.

Yang, H., Bright, J., Kasani, S., Zheng, P., Musho, T., Chen, B., Huang, L., Wu, N., 2019. Metal–organic framework coated titanium dioxide nanorod array p–n heterojunction photoanode for solar water-splitting. Nano Res. 12, 643–650.

Yang, L., Huang, J., Shi, L., Cao, L., Yu, Q., Jie, Y., Fei, J., Ouyang, H., Ye, J., 2017. A surface modification resultant thermally oxidized porous g-C_3N_4 with enhanced photocatalytic hydrogen production. Appl. Catal. B Environ. 204, 335–345. https://doi.org/10.1016/j.apcatb.2016.11.047.

Younis, S.A., Abd-Elaziz, A., Hashem, A.I., 2016. Utilization of a pyrrole derivative based antimicrobial functionality impregnated onto CaO/g-C_3N_4 for dyes adsorption. RSC Adv. 6, 89367–89379. https://doi.org/10.1039/C6RA10143G.

Younis, S., Kim, K.-H., 2020. Heterogeneous photocatalysis scalability for environmental remediation: opportunities and challenges. Catalysts 10, 1109. https://doi.org/10.3390/catal10101109.

Younis, S.A., Kwon, E.E., Qasim, M., Kim, K.-H., Kim, T., Kukkar, D., Dou, X., Ali, I., 2020. Metal-organic framework as a photocatalyst: progress in modulation strategies and environmental/energy applications. Prog. Energy Combust. Sci. 81, 100870 https://doi.org/10.1016/j.pecs.2020.100870.

You, R., Dou, H., Chen, L., Zheng, S., Zhang, Y., 2017. Graphitic carbon nitride with S and O codoping for enhanced visible light photocatalytic performance. RSC Adv. 7, 15842–15850. https://doi.org/10.1039/C7RA01036B.

Yuan, Y.P., Yin, L.S., Cao, S.W., Xu, G.S., Li, C.H., Xue, C., 2015. Improving photocatalytic hydrogen production of metal-organic framework UiO-66 octahedrons by dye-sensitization. Appl. Catal. B Environ. 168–169, 572–576. https://doi.org/10.1016/j.apcatb.2014.11.007.

Zhang, T., Jin, Y., Shi, Y., Li, M., Li, J., Duan, C., 2019. Modulating photoelectronic performance of metal–organic frameworks for premium photocatalysis. Coord. Chem. Rev. 380, 201–229. https://doi.org/10.1016/j.ccr.2018.10.001.

Zheng, L., Xiao, X., Li, Y., Zhang, W., 2017. Enhanced photocatalytic activity of TiO_2 nanoparticles using WS_2/g-C_3N_4 hybrid as co-catalyst. Trans. Nonferrous Met. Soc. China 27, 1117–1126. https://doi.org/10.1016/S1003-6326(17)60130-4.